25. DIAGENESIS AND INTERSTITIAL-WATER CHEMISTRY AT THE PERUVIAN CONTINENTAL MARGIN—MAJOR CONSTITUENTS AND STRONTIUM ISOTOPES[1]

Miriam Kastner,[2] Henry Elderfield,[3] Jonathan B. Martin,[2] Erwin Suess,[4] Keith A. Kvenvolden,[5] and Robert E. Garrison[6]

ABSTRACT

Two distinct hydrogeochemical regimes currently dominate the Peruvian continental margin. One, in shallower water (150–450 m) shelf to upper-slope regions, is characterized by interstitial waters with strong positive chloride gradients with depth. The maximum measured value of 1043 mM chloride at Site 680 at 11°S corresponds to a degree of seawater evaporation of ~2 times. Major ion chemistry and strontioum isotopic composition of the interstitial waters suggest that a subsurface brine that has a marine origin and is of pre-early Miocene "age," profoundly influences the chemistry and diagenesis of this shelf environment. Site 684 at ~9°S must be closest to the source of this brine, which becomes diluted with seawater and/or interstitial water as it flows southward toward Site 686 at ~13°S (and probably beyond) at a rate of approximately 3 to 4 cm/yr, since early Miocene time.

The other regime, in deep water (3000–5000 m) middle to lower-slope regions, is characterized by interstitial waters with steep negative and nonsteady-state chloride gradients with depth. The minimum measured value of 454 mM chloride, at Site 683 at 11°S, corresponds to ~20% dilution of seawater chloride The most probably sources of these low-chloride fluids are gas hydrate dissociation and mineral (particularly clay) dehydration reactions. Fluid advection is consistent with (1) the extent of dilution shown in the chloride profiles, (2) the striking nonsteady-state depth profiles of chlorides at Sites 683 and 688 and of $^{87}Sr/^{86}Sr$ ratios at Site 685, and (3) the temperatures resulting from an average geothermal gradient of 50°C/km and required for clay mineral dehydration reactions. Strontium isotope data reveal two separate fluid regimes in this slope region: a more northerly one at Sites 683 and 685 that is influenced by fluids with a radiogenic continental strontium signature, and a southerly one at Sites 682 and 688 that is influenced by fluids with a nonradiogenic oceanic signatures. Stratigraphically controlled fluid migration seems to prevail in this margin.

Because of its special tectonic setting, Site 679 at 11°S is geochemically distinct. The interstitial waters are characterized by seawater chloride concentrations to ~200 mbsf and deeper by a significantly lower chloride concentration of about two-thirds of the value in seawater, suggesting mixing with a meteoric water source.

Regardless of the hydrogeochemical regime, the chemistry and isotopic compositions of the interstitial waters at all sites are markedly modified by diagenesis, particularly by calcite and dolomite crystallization.

INTRODUCTION

The main incentive for this study of the chemical and isotopic compositions of the interstitial waters obtained during Ocean Drilling Program Leg 112 was to acquire new and deeper insights into the hydrogeological system along the Peruvian margin, where plate convergence is rapid (>4 cm/yr). Convergent plate margins constitute the most important environments of dynamic tectonics on Earth. They are typified by large-scale fluid fluxes, enhanced fluid-solid (sediment and rock) reactions, e.g., consolidation and deformation (Cloos, 1984; Bray and Karig, 1985, 1986; Fowler et al., 1985; Moore, Mascle, et al., 1987), as well as by perturbation of the geothermal regime (Reck, 1987). Extensive venting of fluids manifested by dense benthic communities and/or mud volcanoes, was recently documented off the Oregon-Washington coast (Kulm et al, 1986; Suess et al., 1985; Ritger et al., 1987), Japan Trench (Boulegue et al., 1987), and seaward of the Barbados Ridge accretionary complex (Langseth et al., 1988).

TECTONIC AND STRATIGRAPHIC SETTING

Presumably since the early Mesozoic, the Peru continental margin has evolved in a convergent tectonic regime characterized by subduction, magmatism, erosion, and accretion. The oldest sediments recovered during Leg 112 in the middle to lower-slope sites are of Eocene age, the time when the present-day configuration of the margin evolved (Noble et al., 1979). Benthic foraminifers indicate that the Eocene sediments sampled at a water depth of 3.5 to 5 km were deposited in shelf to upper-slope environment (Suess, von Huene, et al., 1988). Thus, the Peruvian slope region has subsided at least 4 km during the past 40 m.y. Based on extensive geophysical studies, this margin is marked by an Oligocene through early Miocene regional unconformity, and the continental crust underlying the Eocene sediments extends seaward to at least 15 to 20 km east of the trench axis (e.g., Hussong et al., 1976; Hussong and Wipperman, 1981; Kulm et al., 1981; Thornburg and Kulm, 1981; von Huene et al., 1985; Kulm et al., 1986; Miller et al., 1986; Suess, von Huene, et al., 1988). Extensional faulting and tectonic erosion dominated this margin to late Miocene or early Pliocene, after which the relatively minor accretionary complex evolved in the lower slope during the last 6 to 7 m.y. north of ~10°S and during the last ~3 m.y. at ~12°S (von Huene and Miller, 1988). On the landward slope of the margin, the average heat flow (HF) of 40 to 50 mW/m² is higher than in other subduction zones, except for the Nankai Trough (Yamano and Uyeda, this volume).
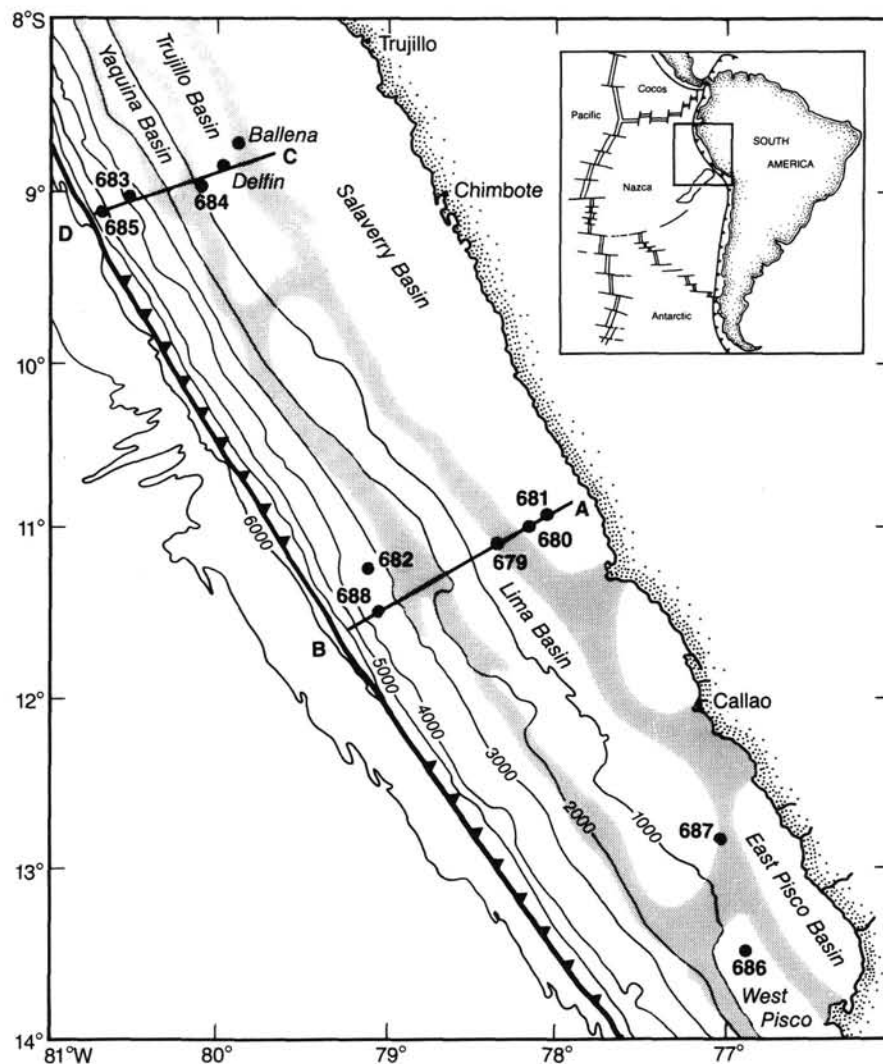
Figure 1. Map of Peru Margin showing locations of sites drilled and transects investigated (C-D and A-B) during Leg 112. Bathymetry in meters. Modified from Thornburg and Kulm (1981).

The sedimentary record in the forearc shelf basins indicates that the oceanographic-sedimentologic regime of intense upwelling, primary productivity, and organic-rich sediment deposition, which dominates the modern shelf to upper-slope region, developed in late Neogene and has been active since (Suess, von Huene, et al., 1988). Ten sites were drilled during Leg 112: three in the northern central Peru margin (~9°S), five in the southern central Peru margin (~11°S), and two farther south (~13°S) in the West Pisco Basin. The locations of the sites are shown in Figure 1. The respective water depths and maximum sediment ages are summarized in Table 1.

Manifestations of overpressured pore fluids and of venting and migrating of fluids have been documented; for example, fluid-escape structures were observed in cores from all sites (Suess, von Huene, et al., 1988; Thornburg and Suess; Suess, von Huene, et al., this volume) and *Calyptogena* sp. clams were dredged from the landward slope zone (Kulm et al., 1986). On the basis of chemical and isotopic analyses of the pore fluids, two distinct hydrogeochemical regimes presently dominate these margin sediments. One regime, in the shallower water (150–450 m) shelf to upper-slope regions, is characterized by strong positive chloride (Cl⁻) gradients with depth. The other regime, in the deeper water (3000–5000 m)

middle to lower-slope regions, is characterized by the presence of low-chloride fluids. Evidence for fluid flow in each of the two hydrogeochemical regimes is noticeable in the interstitial-water chemical and isotopic data in Tables 2 to 11, and illustrated in Figures 2 to 12.

Thus, for the purpose of discussion, the results of the shallow-water sites (680, 681, 684, 686, and 687) and of the

Table 1. Location, water depth, and oldest sediment age of Leg 112 drill sites.

Drill site	Latitude (S)	Longitude (W)	Water depth (m)	Age of oldest sediment
684	08°59.6′	79°54.4′	427	middle Miocene
681	10°58.6′	77°57.5′	151	Pleistocene
680	11°03.9′	78°04.7′	253	early Pliocene
687	12°51.8′	76°59.4′	307	Pliocene
686	13°28.4′	76°53.5′	447	Pleistocene
679	11°03.8′	78°16.3′	450	middle Miocene
683	09°01.7′	80°24.4′	3072	middle Eocene
685	09°06.8′	80°35.0′	5071	late Miocene
682	11°16.0′	79°03.7′	3789	Eocene
688	11°32.3′	78°56.6′	3820	Eocene

Table 2. Interstitial-water chemistry, Shelf Site 680.

Core, section, interval (cm)	Depth (mbsf)	pH	Alkalinity (mM)	Salinity (g/kg)	Cl (mM)	SO$_4$ (mM)	NH$_4$ (mM)	PO$_4$ (μM)	Ca (mM)	Mg (mM)	Mg/Ca ratio	Sr (μM)	K (mM)	Na (mM)	Na/Cl ratio	H$_4$SiO$_4$ (μM)
680C-1H-1, 130–135	1.3	7.8	16.69	34.2	556.2	25.3	1.71	17.4	9.5	52.9	5.59	—	—	—	—	955
B-1H-2, 145–150	3.0	7.7	16.81	34.5	560.0	19.4	2.26	17.6	8.5	53.1	6.23	65	10.9	479	0.86	873
C-1H-3, 145–150	4.5	7.7	15.69	34.5	564.7	20.6	1.68	15.1	8.0	52.4	6.52	67	11.1	488	0.86	936
C-2H-3, 140–150	10.2	7.3	16.46	34.5	583.7	18.1	2.17	—	8.5	49.6	5.82	79	11.0	507	0.87	1068
C-3H-2, 145–150	18.3	7.7	19.05	35.2	595.1	12.6	2.65	—	8.4	49.2	5.86	91	11.2	510	0.86	990
B-3H-3, 145–150	19.5	7.1	19.73	35.2	602.7	11.0	2.54	—	8.2	48.0	5.85	90	10.7	518	0.86	1083
B-6H-3, 145–150	47.5	7.6	15.62	38.0	643.5	6.0	4.05	—	9.8	52.5	5.33	208	11.8	530	0.82	1118
B-8H-1, in-situ	62.5	7.7	12.81	39.8	657.7	10.1	4.24	12.1	12.3	56.3	4.57	—	—	—	—	992
B-9H-4, 145–150	77.9	7.3	8.95	43.8	747.9	12.3	4.93	5.4	14.4	62.0	4.30	249	12.0	611	0.82	1081
B-23H-1, in-situ	195.5	7.2	4.54	64.0	1043.0	37.9	5.19	3.9	35.7	109.5	3.07	429	12.3	815	0.78	871

Table 3. Interstitial-water chemistry, Shelf Site 681.

Core, section, interval (cm)	Depth (mbsf)	pH	Alkalinity (mM)	Salinity (g/kg)	Cl (mM)	SO$_4$ (mM)	NH$_4$ (mM)	PO$_4$ (μM)	Ca (mM)	Mg (mM)	Mg/Ca ratio	Sr (μM)	K (mM)	Na (mM)	Na/Cl ratio	H$_4$SiO$_4$ (μM)
681C-1H-1, 145–150	1.5	7.5	22.28	34.2	557.1	15.5	2.62	25.0	9.4	52.3	5.54	75	11.9	472	0.85	992
B-1H-2, 145–150	3.0	7.9	21.82	36.0	563.7	17.3	2.18	16.7	8.7	50.9	5.84	66	10.5	488	0.97	938
C-1H-3, 145–150	4.5	7.8	17.74	34.5	558.1	15.0	1.74	—	8.2	50.7	6.21	69	10.2	476	0.85	968
C-2H-1, 140–150	7.4	7.8	15.95	34.8	562.8	15.3	2.15	—	8.6	50.4	5.84	77	9.3	480	0.85	1007
C-2H-4, 145–150	11.9	7.7	14.87	34.9	574.2	12.8	1.59	—	8.6	48.9	5.72	84	11.7	486	0.85	1031
B-3H-3, 145–150	19.8	7.5	16.66	35.8	608.3	—	2.51	13.6	7.9	46.8	5.94	96	10.6	—	—	999
C-4H-2, 145–150	27.9	7.7	19.50	36.5	630.1	1.2	3.16	—	7.8	45.8	5.87	178	10.3	531	0.84	1072
C-4H-5, 145–150	32.4	7.7	18.74	37.0	646.2	0	3.51	—	7.8	45.9	5.88	222	10.9	543	0.84	1055
C-5H-3, 145–150	38.9	7.6	18.05	38.0	655.6	0	3.81	—	8.5	46.7	5.46	248	11.2	548	0.84	1118
C-7H-2, 140–150	56.3	7.6	16.84	43.8	731.4	0	4.72	6.0	11.0	54.1	4.94	335	11.2	602	0.82	1075
A-7H-1, in-situ	63.5	7.3	18.21	43.8	770.3	0	4.73	—	12.0	55.9	4.66	337	10.8	637	0.83	1112
C-8H-2, 145–150	65.8	7.4	16.44	45.2	766.6	0	5.02	6.6	12.1	57.2	4.73	389	11.0	628	0.82	1081
B-8H-1, in-situ	67.0	7.5	18.32	43.7	765.9	0	5.17	—	11.8	57.1	4.85	375	10.7	630	0.82	1117
B-9H-1, 140–150	73.8	7.4	15.73	46.0	794.9	0	5.50	5.1	12.8	60.1	4.69	397	11.1	647	0.81	1081
C-9H-2, 140–150	75.3	7.6	15.93	51.5	786.4	0	4.88	5.4	13.4	60.4	4.49	367	11.7	637	0.81	1062
B-12X-3, 140–150	98.9	7.3	13.99	52.3	914.3	2.7	4.56	6.8	17.9	73.3	4.10	416	10.6	735	0.80	1142
B-15X-1, 135–145	126.0	7.3	10.99	57.8	989.2	10.7	4.56	5.1	23.4	83.6	3.57	305	10.1	792	0.80	1001

Table 4. Interstitial-water chemistry, Shelf Site 684.

Core, section, interval (cm)	Depth (mbsf)	pH	Alkalinity (mM)	Salinity (g/kg)	Cl (mM)	SO$_4$ (mM)	NH$_4$ (mM)	PO$_4$ (μM)	Ca (mM)	Mg (mM)	Mg/Ca ratio	Sr (μM)	K (mM)	Na (mM)	Na/Cl ratio	H$_4$SiO$_4$ (μM)
684B-1H-3, 145–150	4.5	7.6	12.82	34.5	557.1	17.7	2.03	5.7	8.5	51.1	5.99	59	11.1	473	0.85	1095
C-1H-3, 145–150	4.5	—	12.33	34.5	558.1	17.6	2.09	16.6	8.5	51.0	6.01	67	10.8	—	—	1109
C-2H-3, 145–150	12.3	7.8	18.66	35.0	575.2	7.1	4.03	11.6	6.4	48.2	7.48	75	11.5	483	0.84	1167
B-3H-3, 145–150	21.5	7.7	22.58	38.2	638.2	1.7	5.53	—	8.0	52.8	6.60	217	12.5	524	0.82	1136
C-3H-3, 145–150	21.8	7.8	22.26	37.9	646.8	2.0	5.36	—	7.5	52.0	6.91	229	12.3	536	0.83	1077
C-4H-6, 145–150	35.8	7.8	23.85	41.8	694.5	0.8	6.64	—	10.4	57.5	5.51	515	13.9	563	0.81	1055
C-5H-1, 145–150	37.8	7.8	23.56	42.5	724.9	0.1	6.53	—	11.1	60.1	5.42	556	13.8	585	0.81	1082
C-6X-1, 145–150	40.5	7.4	23.51	44.0	755.6	0	7.20	—	12.3	60.7	4.93	658	14.2	610	0.81	1136
C-7X-2, 145–150	51.5	7.6	21.19	46.4	778.1	0	9.16	—	15.2	62.7	4.14	772	15.2	618	0.79	—
C-8X-2, 92–97	60.4	7.5	15.66	50.5	861.0	0	10.23	8.1	18.7	66.6	3.56	806	14.9	679	0.79	1181
C-10X-1, 35–40	77.4	7.6	17.33	51.7	932.2	0	12.22	10.1	23.1	69.8	3.02	873	15.7	734	0.79	1115
C-11X-1, 145–150	88.0	7.5	17.50	55.8	944.9	0	12.61	9.4	26.9	71.5	2.66	—	—	—	—	1152
C-13X-1, 140–145	106.9	7.3	12.95	59.7	1028.8	0	14.20	4.6	28.6	74.2	2.60	1401	17.9	801	0.78	1051

Table 5. Interstitial-water chemistry, Shelf Site 686.

Core, section, interval (cm)	Depth (mbsf)	pH	Alkalinity (mM)	Salinity (g/kg)	Cl (mM)	SO$_4$ (mM)	NH$_4$ (mM)	PO$_4$ (μM)	Ca (mM)	Mg (mM)	Mg/Ca ratio	Sr (μM)	K (mM)	Na (mM)	Na/Cl ratio	H$_4$SiO$_4$ (μM)
686B-1H-3, 145–150	4.5	7.9	10.60	35.1	542.8	19.1	1.39	66.0	9.0	48.6	5.43	66	11.4	464	0.85	904
B-2H-3, 145–150	13.0	8.0	25.84	33.8	548.5	1.8	6.67	76.7	5.5	40.5	7.33	76	12.0	467	0.85	985
B-3H-3, 145–150	22.5	8.0	27.12	33.8	554.2	0	7.36	81.6	5.0	36.1	7.30	100	12.2	480	0.87	1029
B-5H-3, 145–150	41.5	8.0	33.96	34.2	557.1	0	13.07	74.8	5.3	33.3	6.26	123	12.3	489	0.88	1040
B-6X-2, 145–150	49.5	7.9	38.06	34.6	569.5	0	15.84	83.5	5.3	32.7	6.13	—	—	—	—	1123
B-9X-6, 145–150	84.0	7.8	54.28	36.4	578.1	0	26.65	66.0	5.6	30.7	5.45	169	12.9	520	0.90	1046
B-12X-2, 145–150	106.5	8.0	56.71	37.5	588.6	0	31.60	63.1	5.7	26.7	4.70	186	13.9	536	0.91	1089
A-14X-1, in-situ	110.7	—	59.09	37.8	604.8	0	32.13	88.4	5.7	26.6	4.66	192	16.6	—	—	1085
B-15X-5, 140–150	139.5	7.8	61.30	38.7	601.0	0	37.67	64.1	6.0	28.0	4.70	207	13.2	544	0.91	1081
B-18X-4, 140–150	166.4	7.8	63.58	39.9	626.7	0	40.00	66.0	7.2	27.7	3.85	263	14.0	567	0.90	1081
A-22X-1, in-situ	186.7	7.8	66.48	40.2	645.8	0	42.15	86.4	8.4	24.9	2.99	311	15.3	589	0.91	1091
B-24X-2, 140–150	220.4	7.9	59.57	41.8	638.2	0	44.66	76.7	7.6	27.0	3.55	479	21.7	563	0.88	1240
B-28X-5, 140–150	262.9	7.9	54.89	42.3	686.8	0	43.90	73.8	8.3	24.5	2.95	367	19.0	614	0.89	1166
B-30X-4, 140–150	280.4	8.1	53.15	43.7	707.8	0	43.38	75.7	9.2	27.3	2.98	466	17.0	629	0.89	1112
B-32X-2, 140–150	296.4	8.4	49.66	43.9	718.3	0	45.13	73.8	9.3	27.1	2.91	511	18.6	635	0.88	1164

Table 6. Interstitial-water chemistry, Shelf Site 687.

Core, section, interval (cm)	Depth (mbsf)	pH	Alkalinity (mM)	Salinity (g/kg)	Cl (mM)	SO₄ (mM)	NH₄ (mM)	PO₄ (μM)	Ca (mM)	Mg (mM)	Mg/Ca ratio	Sr (μM)	K (mM)	Na (mM)	Na/Cl ratio	H₄SiO₄ (μM)
687B-1H-3, 145–150	4.5	7.6	12.24	34.8	547.6	19.3	1.76	49.5	9.3	51.6	5.57	68	14.4	460	0.84	944
B-3H-4, 140–150	20.6	7.8	16.25	34.0	564.7	6.8	3.68	53.4	6.2	43.2	6.94	76	13.6	478	0.85	1038
B-5H-3, 54–64	37.2	7.9	13.57	34.0	580.9	0	12.54	50.5	6.5	35.6	5.50	197	13.6	484	0.83	951
B-7H-1, 140–150	54.1	7.6	10.74	35.0	601.9	0	7.12	53.4	6.7	34.8	5.22	234	13.8	508	0.84	1072
B-15X-1, 140–150	120.7	7.4	12.62	41.6	706.9	0	13.36	56.3	14.3	47.0	3.28	524	15.6	567	0.80	1049
B-19X-3, 103–113	161.3	7.5	11.20	44.9	762.2	0	13.77	59.2	18.8	56.6	3.02	736	13.6	594	0.78	1104
A-19X-1, *in-situ*	169.0	7.3	12.77	46.1	769.9	0	13.83	51.4	20.0	58.9	2.95	768	17.6	592	0.77	1089

Table 7. Interstitial-water chemistry, Shelf Site 679.

Core, section, interval (cm)	Depth (mbsf)	pH	Alkalinity (mM)	Salinity (g/kg)	Cl (mM)	SO₄ (mM)	NH₄ (mM)	PO₄ (μM)	Ca (mM)	Mg (mM)	Mg/Ca ratio	Sr (μM)	K (mM)	Na (mM)	Na/Cl ratio	H₄SiO₄ (μM)
679C-1H-1, 140–150	1.4	7.6	4.81	34.8	555.2	26.5	0.17	4.3	10.7	50.4	4.72	80	10.5	480	0.86	636
D-1H-4, 145–150	5.9	7.5	6.17	34.2	558.0	22.5	0.49	3.9	10.2	52.0	5.11	73	9.6	475	0.85	777
C-1H-4, 140–150	5.9	7.7	6.56	34.9	556.1	25.2	0.44	—	10.7	52.0	4.85	76	10.8	476	0.86	696
C-2H-2, 128–138	11.8	7.3	6.10	33.9	554.2	24.0	0.60	3.0	10.2	50.6	4.95	72	10.3	476	0.86	845
C-3H-1, 140–150	19.9	7.3	7.41	34.2	560.0	23.3	0.80	3.9	10.8	51.0	4.74	78	11.5	478	0.85	1017
D-3H-3, 81–93	21.8	7.6	7.43	34.4	558.1	23.3	0.88	—	10.7	49.9	4.68	69	10.5	479	0.86	1241
C-4H-1, 140–150	29.4	7.5	7.64	34.0	562.9	22.7	0.96	3.2	10.9	50.2	4.60	73	10.6	482	0.86	1224
C-4H-5, 140–150	35.4	7.7	7.83	34.2	564.9	22.2	1.06	3.9	11.0	49.8	4.54	76	9.7	485	0.86	1103
D-6H-3, 140–150	50.3	7.6	8.16	34.0	558.0	20.5	1.45	2.6	10.9	47.1	4.32	87	11.8	478	0.86	1098
C-6H-3, 135–145	51.3	7.7	8.18	34.0	561.9	20.5	1.45	—	10.9	47.5	4.37	80	10.7	482	0.86	1167
C-8H-5, 140–150	73.4	7.6	8.38	34.0	558.0	17.4	1.99	3.5	10.9	44.8	4.13	94	10.9	477	0.85	1237
D-9H-3, 140–150	78.8	7.7	9.08	33.8	558.0	17.0	2.01	3.2	11.0	45.2	4.09	102	11.0	475	0.85	1094
D-17X-1, 140–150	143.8	7.8	11.64	33.0	559.0	7.3	3.73	7.7	11.1	39.5	3.55	198	8.9	472	0.84	1173
D-20X-1, 115–125	172.0	7.6	9.83	31.8	560.9	0	5.28	3.2	15.0	29.8	1.99	484	7.7	467	0.83	1360
E-4X-3, 140–150	275.2	7.6	15.86	22.2	381.0	0	4.84	—	8.6	13.3	1.54	234	4.6	343	0.90	718
E-6X-2†, 140–150	292.7	7.6	16.57	20.1	360.6	0	4.07	0.5	7.0	10.8	1.54	205	4.4	333	0.92	514
E-6X-2‡, 140–150	292.7	7.6	15.52	20.2	358.9	0	4.75	—	6.2	9.1	1.48	229	4.2	335	0.93	307
E-9X-CC†	319.7	7.6	16.99	20.2	338.6	0	4.31	1.3	7.3	8.7	1.19	233	3.6	315	0.93	590
E-12X-1, 140–150	348.2	—	—	20.8	346.7	0	4.63	—	9.0	6.1	0.68	—	—	—	—	836

† Matrix mud
‡ Indurated sediment pieces

Table 8. Interstitial-water chemistry, Slope Site 683.

Core, section, interval (cm)	Depth (mbsf)	pH	Alkalinity (mM)	Salinity (g/kg)	Cl (mM)	SO₄ (mM)	NH₄ (mM)	PO₄ (μM)	Ca (mM)	Mg (mM)	Mg/Ca ratio	Sr (μM)	K (mM)	Na (mM)	Na/Cl ratio	H₄SiO₄ (μM)
683A-1H-1, 145–150	1.5	7.6	4.43	34.2	547.6	30.7	0.50	8.2	9.7	50.9	5.25	69	12.1	479	0.88	684
A-3H-3, 145–150	16.2	7.6	57.40	34.2	524.2	0	6.12	145.8	3.7	50.7	13.79	120	12.6	454	0.87	1072
A-6H-3, 144–150	44.6	7.2	69.95	34.5	524.2	0	11.64	166.3	3.7	50.7	13.82	132	12.7	461	0.88	1028
A-9H-3, 145–150	73.2	7.8	90.74	35.5	527.3	0	16.13	160.0	6.2	54.4	8.77	145	10.2	461	0.89	978
A-12X-4, 135–145	103.1	7.6	98.78	35.5	520.9	0	20.36	160.2	8.1	51.5	6.40	205	13.3	467	0.90	1098
A-15X-1, 140–150	127.1	7.6	99.29	35.0	508.7	0	21.44	128.0	8.5	47.4	5.56	208	13.9	461	0.91	1094
A-18X-3, 145–150	158.7	7.6	92.88	34.2	503.3	0	22.30	137.6	8.9	43.0	4.85	214	12.1	458	0.91	—
A-21X-1, 145–150	184.2	7.5	88.89	32.9	482.1	0	24.54	119.9	7.4	34.0	4.58	211	13.1	451	0.93	1224
A-24X-1, 69–74	211.9	—	80.26	32.0	475.0	0	23.36	54.7	6.4	29.3	4.55	198	13.1	—	—	1398
A-27X-1, 123–128	240.9	7.6	64.56	31.3	474.1	0	19.29	44.7	6.5	26.8	4.10	195	12.7	440	0.93	1375
A-30X-2, 74–79	270.4	7.7	53.22	30.2	477.9	0	15.98	25.4	7.6	27.2	3.56	213	13.1	432	0.90	1229
A-33X-5, 145–150	304.2	—	—	29.8	475.1	0	13.98	16.2	7.4	24.9	3.37	207	13.4	—	—	1180
A-36X-3, 145–150	329.6	7.8	40.01	29.8	474.1	0	10.60	7.9	8.6	25.9	3.01	217	11.2	423	0.89	1236
A-39X-2, 140–150	356.6	7.2	35.50	29.4	473.2	0	10.91	9.5	8.9	23.2	2.60	221	11.8	421	0.89	1412
A-43X-2, 140–150	393.6	7.8	27.07	28.2	471.1	0	9.44	6.8	10.7	20.4	1.90	—	—	—	—	1258
B-2X-2, 140–150	414.9	—	—	28.8	460.7	0	10.13	6.7	11.4	19.6	1.72	—	—	—	—	1348
A-45X-4, 140–150	415.6	7.4	28.96	27.8	457.9	0	7.67	12.8	12.4	19.1	1.54	310	10.2	405	0.89	1229
B-3X-2, 140–150	424.4	7.4	34.90	28.0	456.0	0	9.76	5.8	10.3	18.5	1.79	285	10.5	413	0.91	1337
B-6X-2, 51–63	452.0	7.7	32.28	28.8	454.1	0	8.49	4.6	13.1	16.4	1.25	337	10.1	408	0.90	1252

deep-water sites (682, 683, 685, and 688) are considered separately. Site 679 (450 m water depth), due to its special tectonic setting, is geochemically unusual and is discussed separately. This site is characterized by seawater Cl⁻ values to ~200 mbsf, and below this depth by significantly lower Cl⁻ concentrations, as shown in Figures 7 and 12.

METHODS

Most interstitial waters were obtained by routine shipboard squeezing of whole-round sediment samples (Man-

heim and Sayles, 1974) almost immediately after core retrieval and a few by an *in-situ* water sampler (Barnes, 1988). The sediment samples were squeezed at ambient temperature, using stainless steel squeezers, at pressures of 2000 to 3000 psi (~140–210 kg/cm²). A pressure of 4000 psi (280 kg/cm²) occasionally was used only experimentally for indurated sediment samples, but did not improve the recovery of interstitial waters. The possibility that squeezing clay-rich samples at >2400 psi slightly affects Cl⁻ concentrations due to membrane filtration, suggested by Sayles

Table 9. Interstitial-water chemistry, Slope Site 685.

Core, section, interval (cm)	Depth (mbsf)	pH	Alkalinity (mM)	Salinity (g/kg)	Cl (mM)	SO₄ (mM)	NH₄ (mM)	PO₄ (μM)	Ca (mM)	Mg (mM)	Mg/Ca ratio	Sr (μM)	K (mM)	Na (mM)	Na/Cl ratio	H₄SiO₄ (μM)
685A-1H-2, 145–150	3.0	7.9	15.17	34.0	548.2	21.1	1.15	92.0	8.4	51.6	6.12	66	12.1	472	0.86	919
A-3H-3, 145–150	18.1	7.8	71.42	35.8	555.2	0	7.40	368.0	4.4	60.1	13.65	111	8.9	481	0.87	995
A-6X-4, 145–150	40.1	7.2	118.52	38.2	541.9	0	16.17	409.2	3.8	66.8	17.44	124	16.1	487	0.90	1078
A-9X-7, 145–150	79.6	7.1	142.91	39.8	530.4	0	27.19	597.1	4.2	67.5	15.94	134	16.9	486	0.92	1069
A-12X-5, 145–150	106.6	7.1	155.62	40.0	540.9	0	31.52	826.2	4.2	67.0	16.10	138	16.7	506	0.94	1058
A-15X-4, 140–150	133.5	6.8	156.37	40.3	530.4	0	31.76	755.7	5.3	68.3	12.85	143	16.0	492	0.93	1104
A-18X-6, 145–150	165.1	6.6	146.61	39.8	540.9	0	32.32	526.6	5.1	61.5	11.97	165	18.8	503	0.93	1169
A-27X-1, 120–130	234.8	6.8	78.61	34.5	525.3	0	24.00	146.6	6.5	40.2	6.18	232	18.1	468	0.89	1050
A-30X-2, 127–137	264.9	6.6	76.06	35.0	535.9	0	20.21	121.7	9.3	41.2	4.45	—	—	—	—	1165
A-35X-6, 140–150	318.5	6.8	65.27	34.0	—	0	18.48	—	—	—	—	—	—	—	—	1193
A-36X-6, 140–150	328.0	6.9	64.98	34.2	535.0	0	17.29	92.9	11.4	37.2	3.26	454	15.9	469	0.88	1162
A-44X-3, 40–50	396.0	6.6	36.76	33.5	534.0	0	11.14	94.0	14.4	32.1	2.23	502	11.2	454	0.85	1225
A-47X-1, 128–138	422.4	6.6	—	34.0	—	0	10.93	—	—	—	—	—	—	—	—	1251
A-50X-1, 92–102	450.5	6.8	18.75	33.8	542.6	0	10.58	69.6	17.8	28.2	1.58	699	12.0	446	0.82	997

Table 10. Interstitial-water chemistry, Slope Site 682.

Core, section, interval (cm)	Depth (mbsf)	pH	Alkalinity (mM)	Salinity (g/kg)	Cl (mM)	SO₄ (mM)	NH₄ (mM)	PO₄ (μM)	Ca (mM)	Mg (mM)	Mg/Ca ratio	Sr (μM)	K (mM)	Na (mM)	Na/Cl ratio	H₄SiO₄ (μM)
682A-1H-3, 145–150	4.5	7.7	10.60	34.0	550.5	24.7	0.81	16.8	9.0	50.8	5.64	70	10.7	479	0.87	861
A-3H-3, 140–150	23.7	7.3	29.60	34.0	560.0	12.2	3.03	40.7	5.2	48.9	9.45	62	10.6	492	0.88	1160
A-6H-3, 140–150	52.2	7.3	49.89	34.0	560.6	0	6.82	96.9	5.5	46.4	8.38	131	8.5	491	0.88	1341
A-9X-1, 106–116	77.4	7.4	44.80	33.6	557.7	0	8.38	67.4	6.8	44.6	6.60	—	—	—	—	1381
A-12X-1, 140–150	105.7	7.1	39.95	33.2	556.6	0	9.79	33.6	6.8	42.0	6.16	136	10.2	479	0.86	1100
A-15X-1, 135–139	134.6	6.6	46.89	33.2	546.7	0	11.96	27.7	8.9	39.0	4.39	176	11.2	474	0.87	1462
A-16X-1, in-situ	142.8	7.1	54.74	33.9	552.7	0	13.62	21.7	9.9	39.3	3.96	198	10.9	484	0.88	1344
A-18X-1, 145–150	163.3	6.6	50.47	33.2	545.9	0	13.14	22.6	10.0	38.2	3.81	203	10.4	476	0.87	1375
A-21X-1, 130–135	191.6	7.4	51.04	33.2	532.3	0	14.97	7.7	5.5	40.6	7.39	194	14.1	462	0.87	1477
A-27X-1, 106–111	248.4	6.7	49.22	32.5	532.9	0	15.64	15.7	10.7	34.7	3.25	—	—	—	—	1597
A-34X-2, 140–150	307.5	7.2	46.44	32.0	515.5	0	18.58	7.3	10.8	26.3	2.44	298	9.3	459	0.89	1495
A-36X-1, 140–150	322.1	7.3	34.46	31.0	515.4	0	16.49	6.7	10.5	25.7	2.45	273	10.6	450	0.87	1165
A-46X-1, 140–150	409.6	—	—	30.2	504.0	0	16.25	4.9	15.3	18.8	1.23	—	—	—	—	828

Table 11. Interstitial-water chemistry, Slope Site 688.

Core, section, interval (cm)	Depth (mbsf)	pH	Alkalinity (mM)	Salinity (g/kg)	Cl (mM)	SO₄ (mM)	NH₄ (mM)	PO₄ (μM)	Ca (mM)	Mg (mM)	Mg/Ca ratio	Sr (μM)	K (mM)	Na (mM)	Na/Cl ratio	H₄SiO₄ (μM)
688A-1H-4, 145–150	6.0	8.0	28.44	33.8	563.8	4.5	3.20	45.7	7.2	50.5	7.01	73	18.3	464	0.82	920
A-3H-4, 145–150	23.8	7.8	70.35	36.3	562.9	1.6	10.07	188.0	4.5	53.8	12.11	118	21.3	488	0.87	1078
A-6H-1, in-situ	46.3	8.2	97.96	37.5	550.3	0	18.46	—	4.8	57.7	11.94	161	24.2	481	0.87	1100
A-6H-3, 145–150	50.8	7.7	99.49	37.4	546.5	0	20.90	191.6	4.4	55.4	12.51	123	33.9	472	0.86	1248
A-9X-5, 140–150	82.2	7.6	153.31	40.8	544.5	0	34.24	554.5	4.5	71.2	15.68	124	26.6	486	0.89	1133
A-12X-1, 140–150	104.7	7.8	189.27	44.2	531.1	0	41.18	746.8	5.9	85.4	14.41	137	40.6	457	0.86	1080
A-16X-4, 140–150	147.2	7.4	244.46	47.2	528.2	0	52.07	462.6	7.1	96.5	13.63	163	37.6	476	0.90	1089
A-18X-1, in-situ	160.3	8.0	261.65	49.3	533.9	0	54.98	—	7.6	103.4	13.59	187	51.7	469	0.88	1106
A-19X-3, 140–150	174.2	7.7	264.65	49.0	527.2	0	60.69	303.7	7.3	98.9	13.55	169	45.6	474	0.90	1104
A-21X-3, 108–118	192.9	8.0	265.68	48.3	522.4	0	63.02	175.5	7.2	96.8	13.47	169	34.9	484	0.93	1047
A-25X-1, 140–150	228.2	7.7	250.64	46.2	—	0	—	—	—	—	—	—	—	—	—	—
A-27X-4, 140–150	251.7	8.0	233.33	46.0	520.1	0	58.36	—	6.3	87.1	13.83	145	42.1	468	0.90	1091
A-30X-1, 115–125	275.5	8.2	220.95	44.5	517.6	0	56.65	178.4	5.7	78.6	13.88	146	39.5	477	0.92	1135
A-33X-3, 140–150	307.2	8.0	195.19	43.8	507.9	0	52.53	295.4	6.1	70.1	11.45	147	40.6	459	0.90	1186
E-3R-4, 140–150	365.0	7.7	123.50	36.5	470.8	0	37.36	274.0	2.7	45.2	16.70	128	22.3	439	0.92	1254
E-6R-4, 140–150	393.5	8.0	102.90	34.2	492.0	0	31.82	143.8	3.5	39.2	11.29	124	22.5	456	0.91	1354
E-9R-5, 140–150	422.0	7.9	78.48	32.8	494.1	0	27.57	59.2	5.7	29.5	5.16	160	19.0	456	0.92	1359
E-12R-1, 140–150	450.5	8.1	67.63	32.2	482.5	0	25.36	20.3	8.6	26.5	3.07	167	18.4	437	0.91	1425
E-19R-3, 140–150	521.4	—	—	31.2	489.0	0	16.22	9.6	15.4	24.2	1.57	—	—	—	—	1381
E-23R-1, 140–150	556.4	—	—	30.0	486.1	0	10.80	7.7	18.7	22.2	1.19	—	—	—	—	1012
E-27R-1, 140–150	594.4	—	—	30.2	502.1	0	—	—	25.7	20.3	0.79	—	—	—	—	639

(1970), was re-investigated by Gieskes et al., (in press), who did not observe any significant effect up to pressures of 3000 psi.

The methods used for the shipboard analyses of pH, alkalinity, salinity, Cl⁻, calcium (Ca^{2+}), magnesium (Mg^{2+}), sulfate (SO_4^{2-}), ammonia (NH_4^+), phosphate (PO_4^{3-}), and silicate (H_4SiO_4) are described in Gieskes and Peretsman (1986). Strontium (Sr^{2+}) and potassium (K^+) were analyzed by flame atomic absorption spectrometry, and sodium (Na^+) concentrations were calculated from charge balance calculations. For these calculations, ionized ammonia values, at the measured pH values, were used (Whitfield, 1974). Isotope ratios of $^{18}O/^{16}O$, D/H, $^{13}C/^{12}C$, and $^{87}Sr/^{86}Sr$ were determined by mass spectrometry.

To provide an independent check on the calculated Na^+ concentration values, a number of samples were analyzed at Oregon State University by flame atomic absorption spectrophotometry. In addition, K^+ concentrations were measured, using the same technique, for an independent calibration of the data set. Good agreement was generally found in both cases. Further details of these inter-calibrations are given in Suess, von Huene, et al. (this volume).
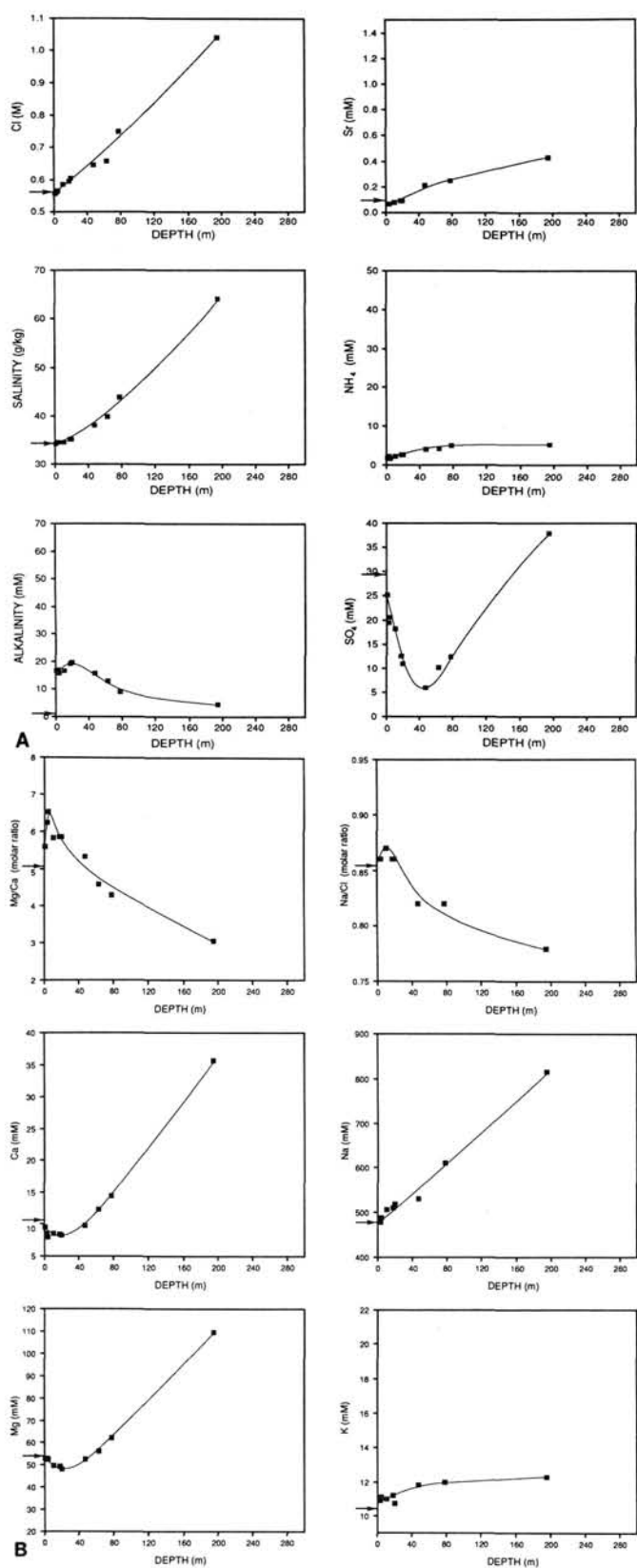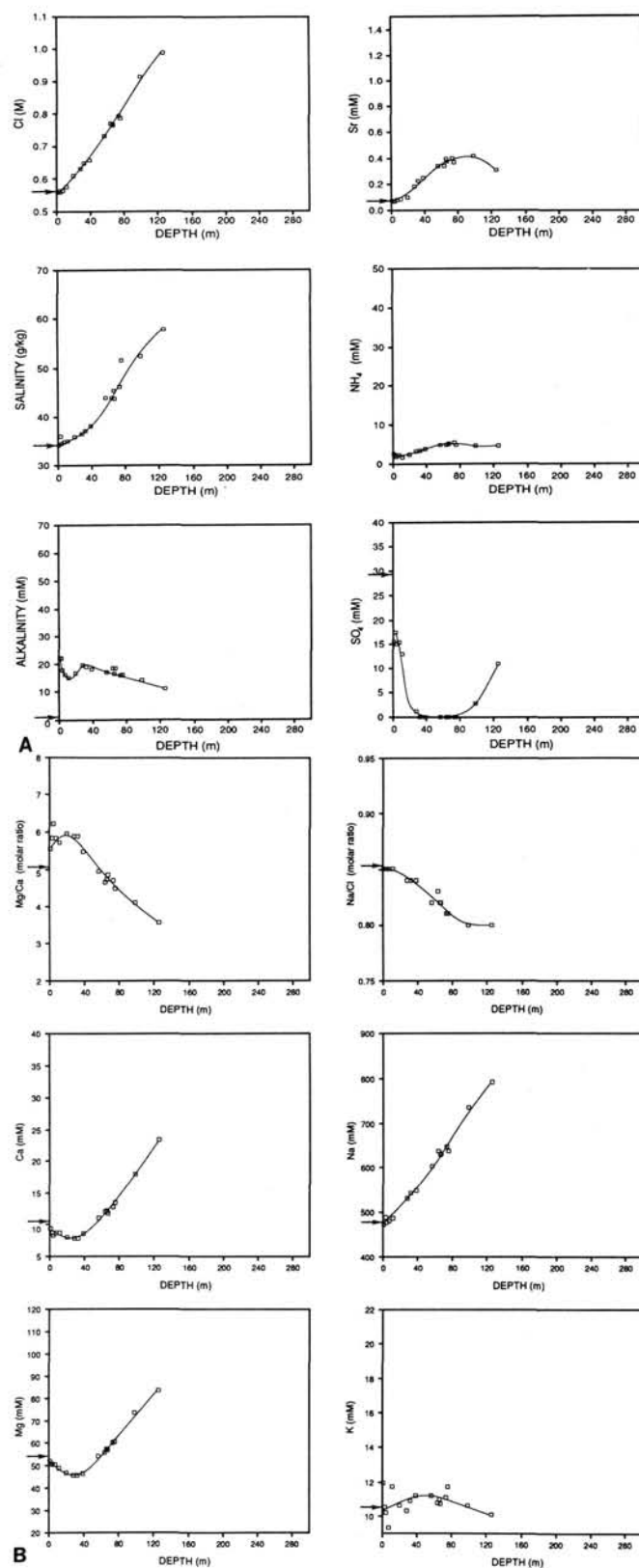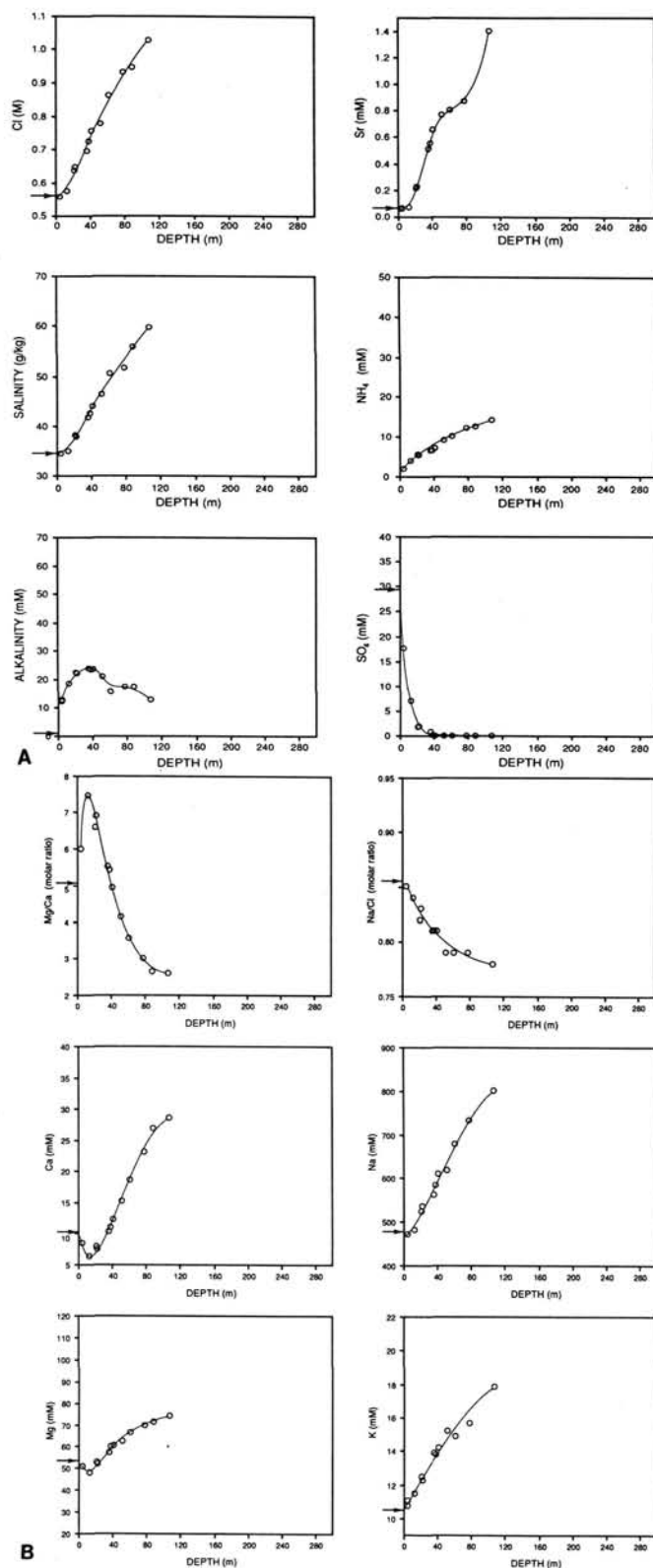
Figure 2. Depth profiles of interstitial-water species for shelf Site 680.
A. chloride, strontium, salinity, ammonia, alkalinity, sulfate. B.
Mg^{2+}/Ca^{2+} molar ratio, Na^+/Cl^- molar ratio, calcium, sodium, magnesium, potassium. Arrows indicate seawater composition.
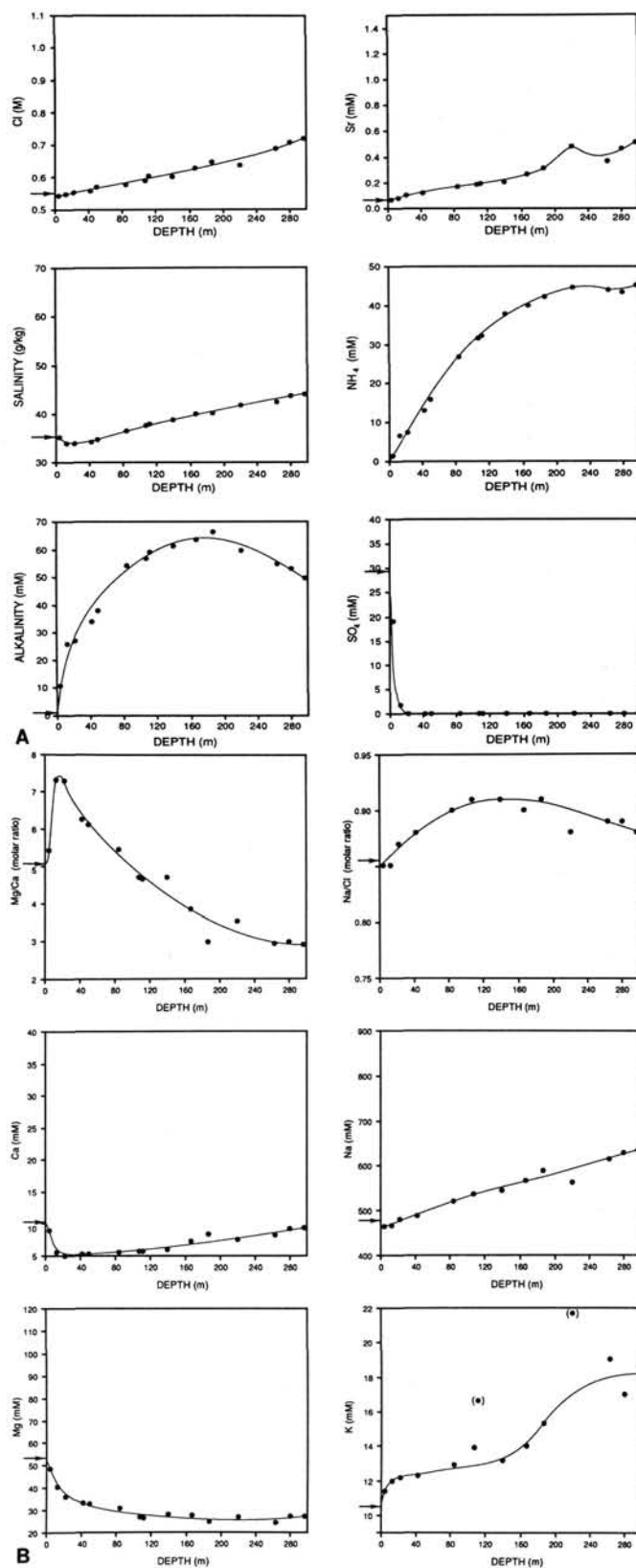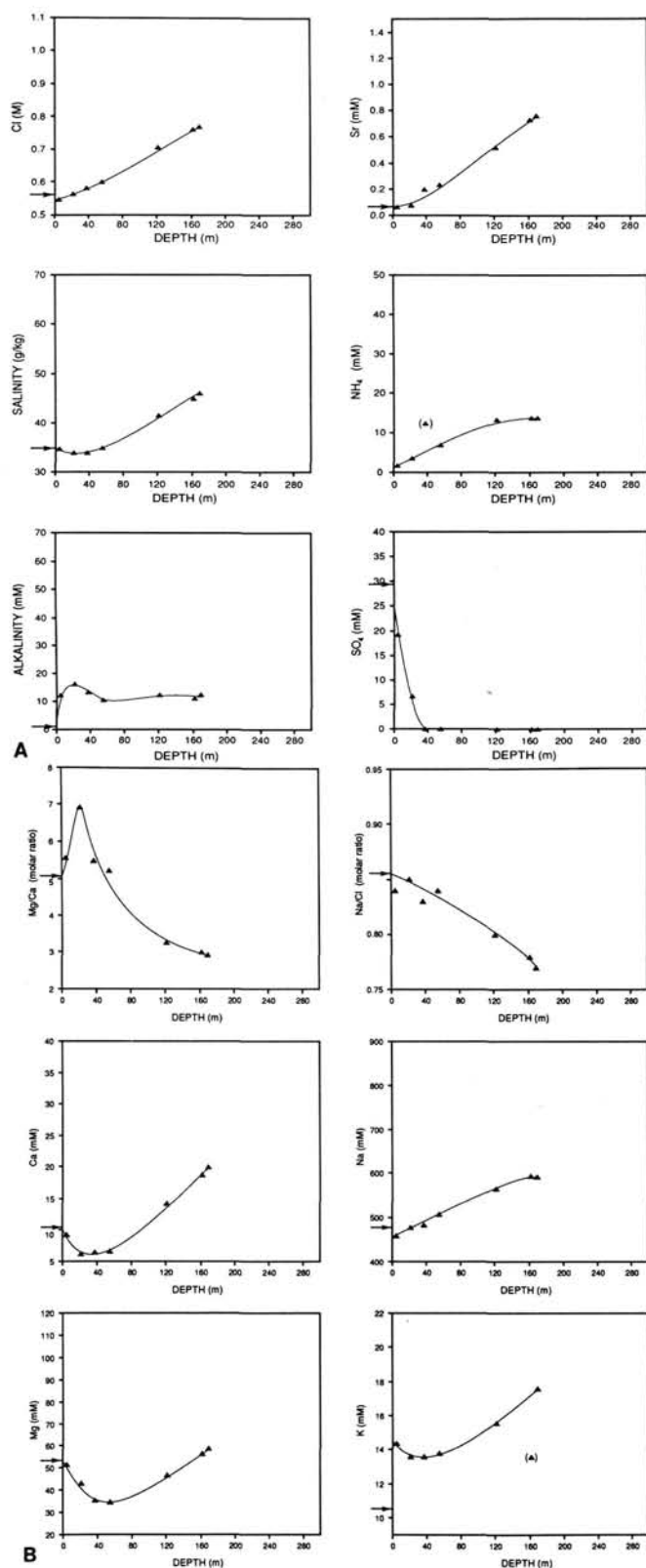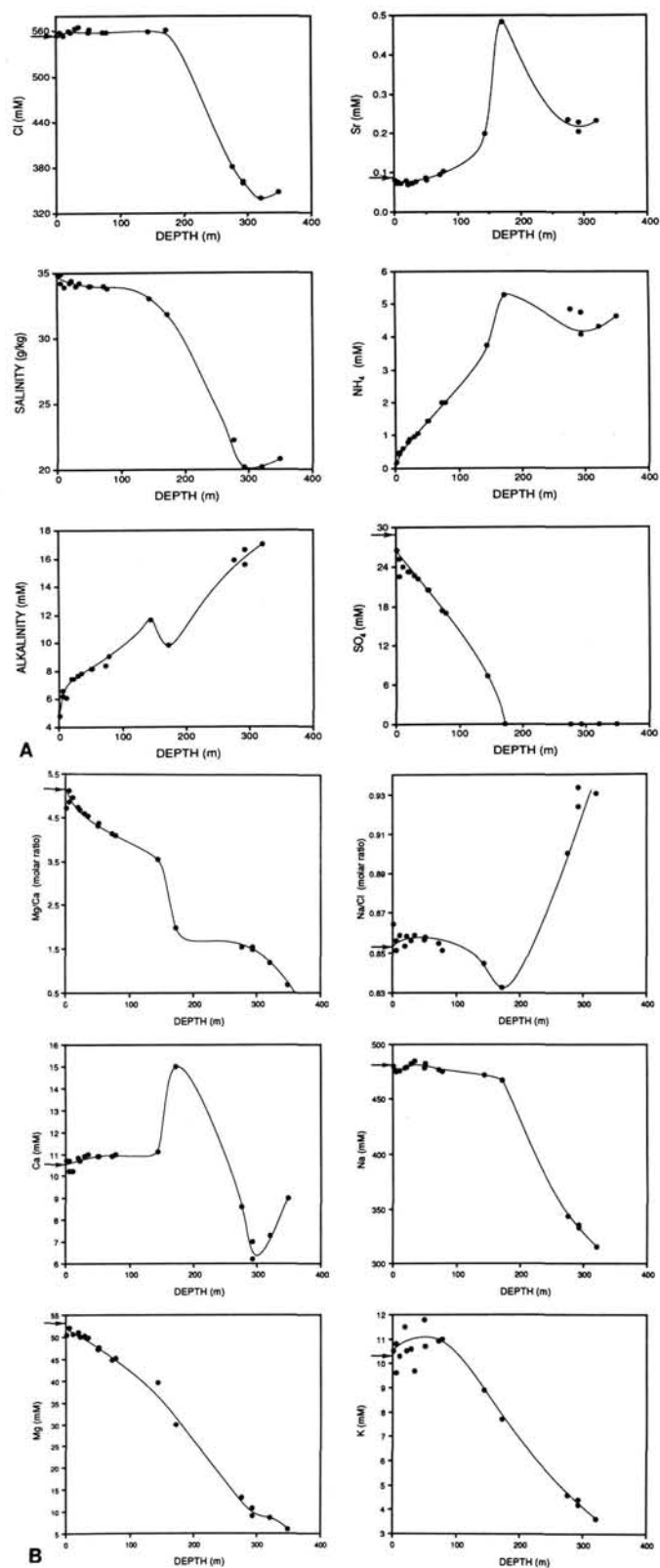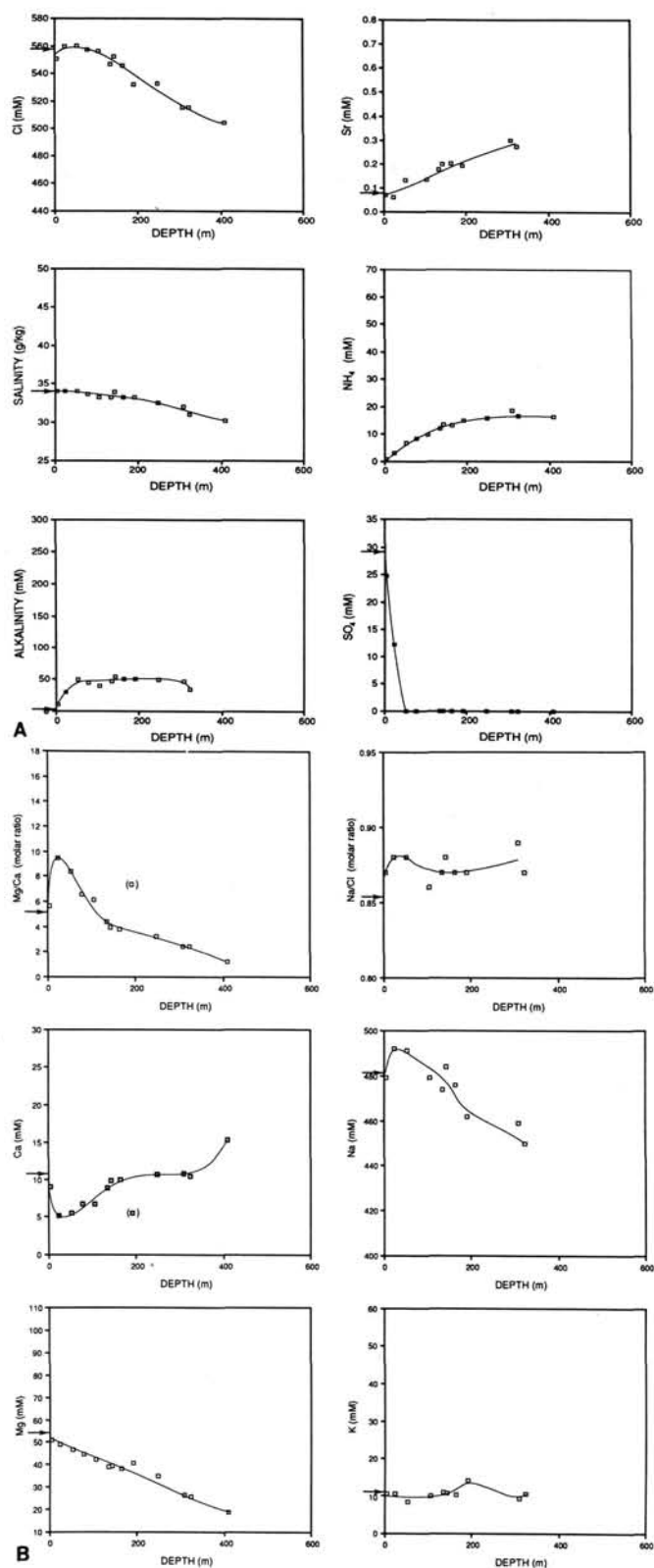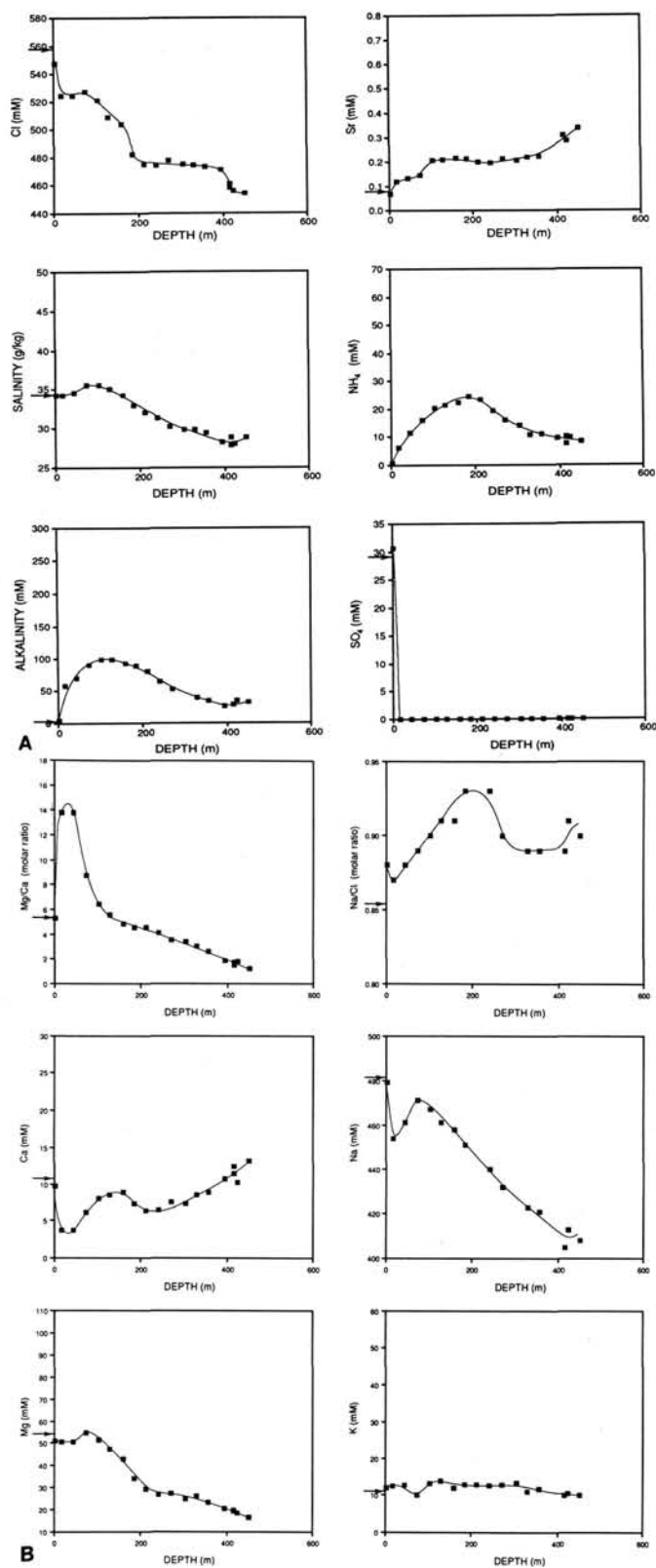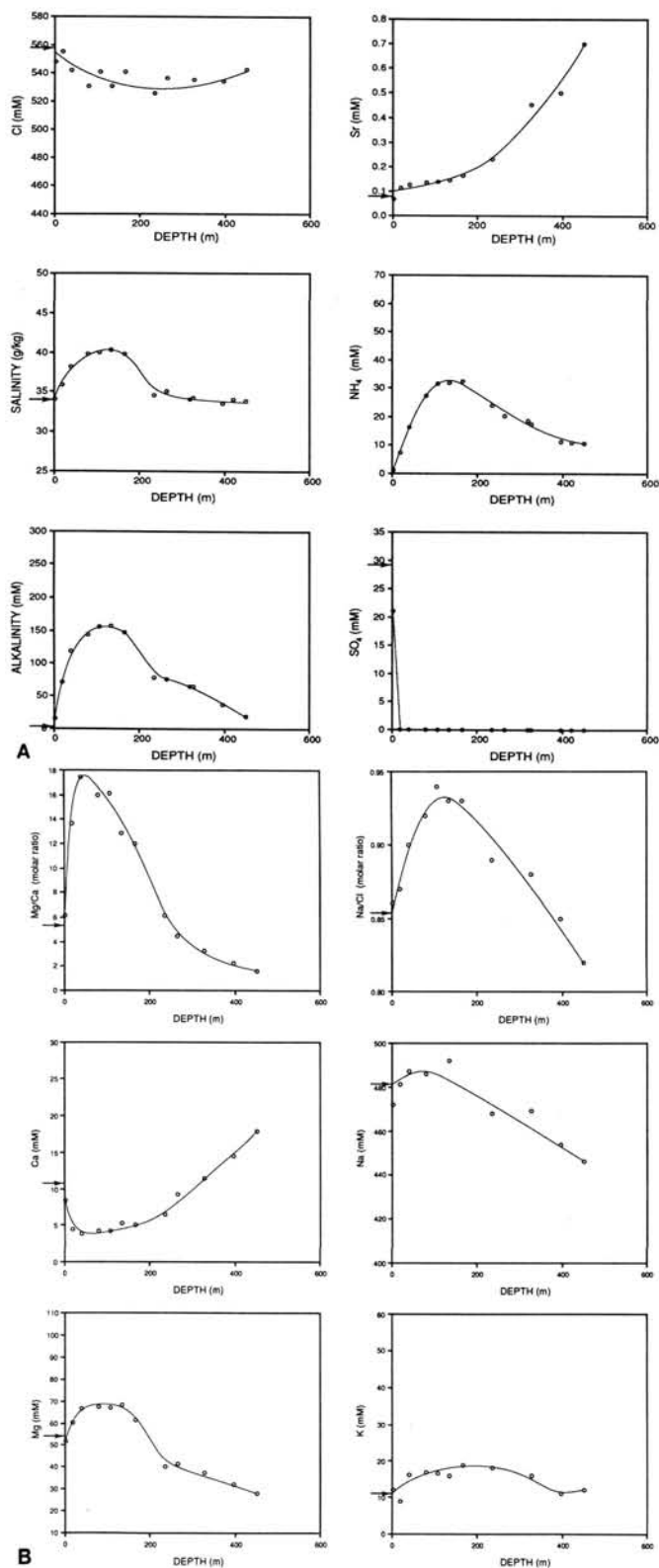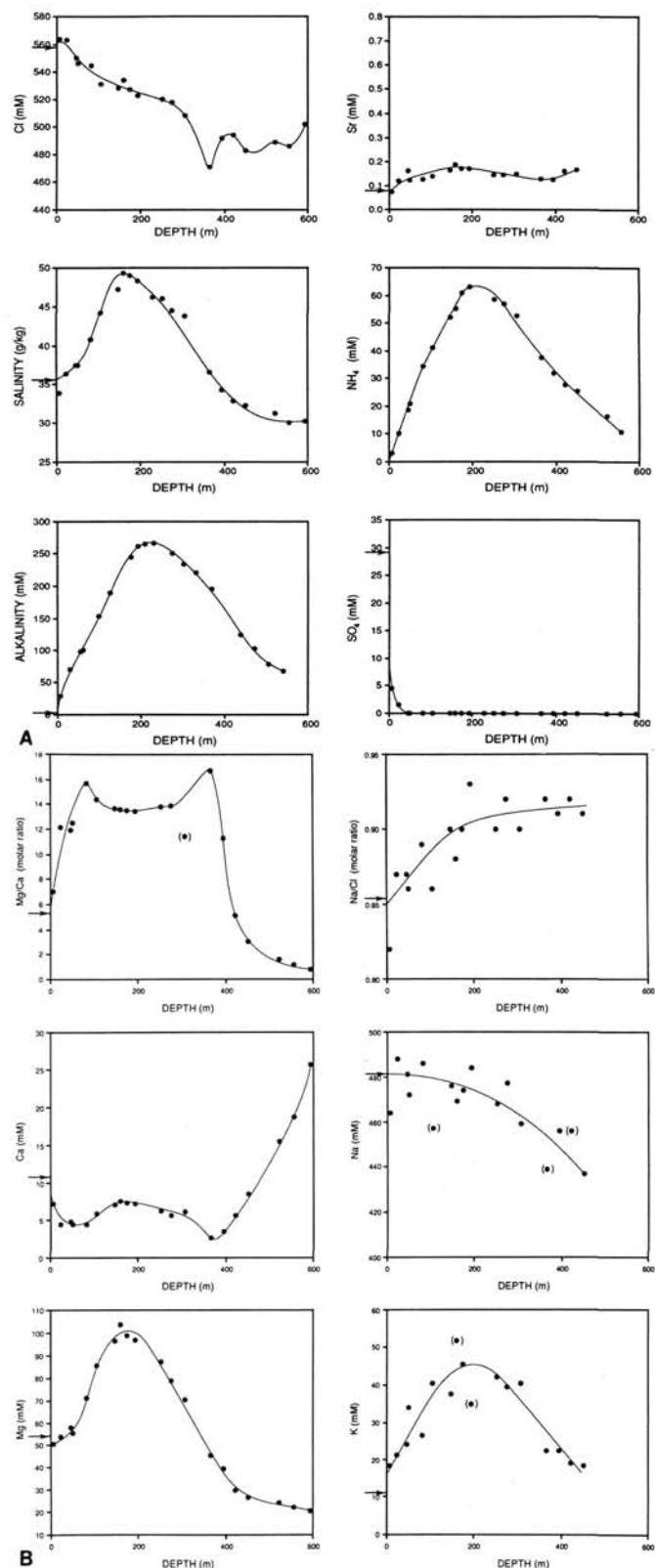
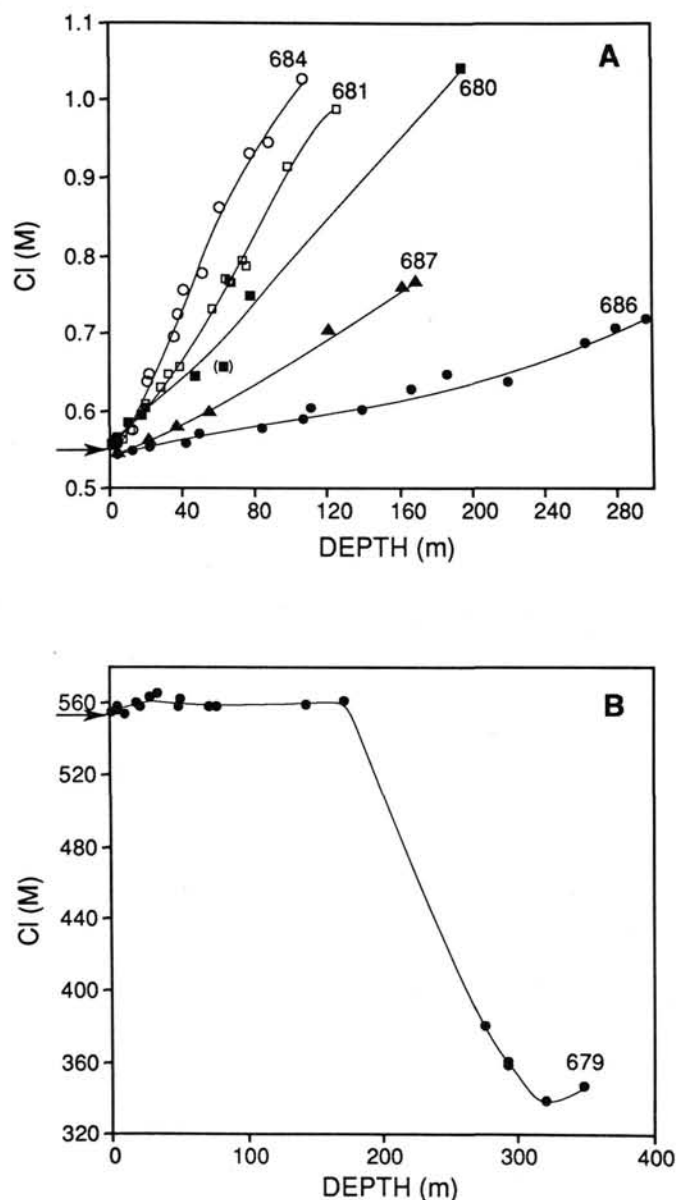Figure 3. Depth profiles of interstitial-water species for shelf Site 681.
A. chloride, strontium, salinity, ammonia, alkalinity, sulfate. B.
Mg^{2+}/Ca^{2+} molar ratio, Na^+/Cl^- molar ratio, calcium, sodium, magnesium, potassium. Arrows indicate seawater composition.

Figure 4. Depth profiles of interstitial-water species for shelf Site 684. A. Chloride, strontium, salinity, ammonia, alkalinity, sulfate. B. Mg^{2+}/Ca^{2+} molar ratio, Na^+/Cl^- molar ratio, calcium, sodium, magnesium, potassium. Arrows indicate seawater composition.

Figure 5. Depth profiles of interstitial-water species for shelf Site 686. A. Chloride, strontium, salinity, ammonia, alkalinity, sulfate. B. Mg^{2+}/Ca^{2+} molar ratio, Na^+/Cl^- molar ratio, calcium, sodium, magnesium, potassium. Arrows indicate seawater composition.

Figure 6. Depth profiles of interstitial-water species for shelf Site 687. A. Chloride, strontium, salinity, ammonia, alkalinity, sulfate. B. Mg^{2+}/Ca^{2+} molar ratio, Na^+/Cl^- molar ratio, calcium, sodium, magnesium, potassium. Arrows indicate seawater composition.

Figure 7. Depth profiles of interstitial-water species for shelf Site 679. A. Chloride, strontium, salinity, ammonia, alkalinity, sulfate. B. Mg^{2+}/Ca^{2+} molar ratio, Na^+/Cl^- molar ratio, calcium, sodium, magnesium, potassium. Arrows indicate seawater composition.

Figure 8. Depth profiles of interstitial-water species for slope Site 682. A. Chloride, strontium, salinity, ammonia, alkalinity, sulfate. B. Mg^{2+}/Ca^{2+} molar ratio, Na^+/Cl^- molar ratio, calcium, sodium, magnesium, potassium. Arrows indicate seawater composition.

Figure 9. Depth profiles of interstitial-water species for slope Site 683. A. Chloride, strontium, salinity, ammonia, alkalinity, sulfate. B. Mg^{2+}/Ca^{2+} molar ratio, Na^+/Cl^- molar ratio, calcium, sodium, magnesium, potassium. Arrows indicate seawater composition.

Figure 10. Depth profiles of interstitial-water species for slope Site 685. A. Chloride, strontium, salinity, ammonia, alkalinity, sulfate. B. Mg^{2+}/Ca^{2+} molar ratio, Na$^+$/Cl$^-$ molar ratio, calcium, sodium, magnesium, potassium. Arrows indicate seawater composition.

Figure 11. Depth profiles of interstitial-water species for slope Site 688. A. Chloride, strontium, salinity, ammonia, alkalinity, sulfate. B. Mg^{2+}/Ca^{2+} molar ratio, Na$^+$/Cl$^-$ molar ratio, calcium, sodium, magnesium, potassium. Arrows indicate seawater composition.

Figure 12. Profiles of chloride concentration in interstitial waters vs. depth. A. Saline Sites 680, 681, 684, 686, 687. B. Shelf Site 679.

Although greatest care was used when preparing sediment samples for squeezing to avoid contamination with seawater introduced by drilling, in several samples some contamination was unavoidable. In the deeper buried, somewhat indurated, fissile or deformed sediments and in the more silty-sandy sediments, in particular in the middle and lower-slope sites, scattered contamination was observed. In the organic-matter-rich sediments of all sites drilled in this margin, the sediments prone to contamination occur at burial depths below the sulfate reduction zone. Contamination by seawater, introduced by drilling, is therefore easily monitored and quantified by sulfate analysis. Except for pH, salinity, and oxygen and hydrogen isotopes, the concentrations of all major constituents of the contaminated samples were corrected for the amount of admixed seawater, using element concentrations in average ocean water (Broecker and Peng, 1982). Appendix 1 lists all Leg 112 uncontaminated interstitial-water samples. Appendix 2 lists all interstitial-water samples corrected for admixed seawater introduced by drilling and the calculated percentage of admixed

Table 12. Strontium isotopic composition of interstitial waters, Leg 112.

Core, section	Depth (mbsf)	Ratio	2σSD $\pm$
112-679D-3H-3	21.8	0.709092	30
679D-9H-3	78.8	0.708923	32
679D-20X-1	172.0	0.708749*	32
679E-4X-3	275.2	0.708526*	24
679E-9X-CC	319.7	0.708402*	36
679E-12X-1	348.2	0.708392*	26
680B-1H-2	3.0	0.709097	28
680C-2H-3	10.2	0.709044	28
680C-3H-2	18.3	0.708881	42
680B-6H-3	47.5	0.708911	46
680B-9H-4	77.9	0.709311	38
681B-1H-2	3.0	0.709111	28
681C-2H-4	11.9	0.709001	26
681C-5H-3	38.9	0.708804	28
681B-9H-1	73.8	0.708612	46
681B-12X-3	98.9	0.708438	32
681B-15X-1	126.0	0.708326	30
682A-1H-3	4.5	0.709163	32
682A-6H-3	52.2	0.709021*	32
682A-12X-1	105.7	0.708816*	38
682A-18X-1	163.3	0.708666*	26
682A-34X-2	307.5	0.708186*	30
682A-46X-1	409.6	0.707218*	32
683A-3H-3	16.2	0.709087*	30
683A-9H-4	73.2	0.709002	26
683A-15X-1	127.1	0.708704*	28
683A-30X-2	270.4	0.708546	36
683B-3X-2	424.4	0.708740	24
683B-6X-2	452.0	0.708936	42
684B-1H-3	4.5	0.709085	42
684B-3H-3	21.5	0.708533	26
684C-5H-1	37.8	0.708395	36
684C-7X-2	51.5	0.708301*	24
684C-10X-1	77.4	0.708203*	32
684C-13X-1	106.9	0.708265	28
685A-9X-7	79.6	0.709946	22
685A-18X-6	165.1	0.709205	42
685A-27X-1	234.8	0.709554	34
685A-36X-6	328.0	0.709958	26
685A-50X-1	450.5	0.709708	28
686B-1H-3	4.5	0.709112	38
686B-3H-3	22.5	0.708989	42
686B-5H-3	41.5	0.709027	
686B-15X-5	139.5	0.708906	36
686B-32X-2	296.4	0.708993	52
687B-1H-3	4.5	0.709161	42
687B-3H-4	20.6	0.709003	20
687B-6H-5	50.6	0.708874	14
687B-7H-1	54.1	0.708870	16
687B-15X-1	120.7	0.708859	16
688A-3H-4	23.8	0.709135	10
688A-12X-1	104.7	0.709033	34
688A-19X-3	174.2	0.709010	30
688A-33X-3	307.2	0.708835	40
688E-3R-4	365.0	0.708460	11
688E-6R-4	393.5	0.708300*	28

*Corrected for admixed seawater introduced by drilling.

seawater. Tables 2 through 12 include the corrected concentrations and isotopic values.

THE SHELF SITES

The most distinctive characteristic of the hydrogeochemical regime at the shelf sites is the strong positive Cl^- gradients with depth. The maximum measure value of 1043 mM Cl^- at Site 680, at ~200 mbsf, corresponds to a degree of seawater evaporation of ~2 times. The steepest Cl^- gradient, observed at Site 684, reaches 1029 mM at ~100 mbsf. The magnitude of the depth gradients decreases systematically from the northernmost (9°S) to the southernmost (13°S) sites, in the following sequence:

$$684 > 681 > 680 > 687 > 686.$$

This systematic change of gradients is illustrated in Figure 12A. The Cl⁻ gradients appear to be diffusive profiles between seawater and a subsurface brine, located at a depth beyond that reached by drilling at any of the sites. Thus, the areal extent of the subsurface brine is large, at least 25×10^3 km². Except for Site 686, the Cl⁻ depth profiles are essentially linear below 20 to 40 mbsf. As a simple approximation, we assumed that the observed Cl⁻ profiles reflect mixing between the two end-members, a deep-seated brine, and seawater.

A comprehensive evaluation of the depth profiles of additional ions and of stable isotopes, e.g., of strontium, oxygen, and hydrogen, that may be affected or even controlled by the presence of the subsurface brine, should help to elucidate its origin, the chemistry of the end-member brine, and possibly the age and location of the source.

Possible origins of this brine are (1) subsurface dissolution of evaporite minerals, especially of halite (NaCl), by meteoric or seawater; or (2) incursion of a dense marine or mixed marine/meteoric brine from either a Holocene or an ancient coastal intertidal and supratidal or lagoonal evaporitic system.

The Bocana de Virrila, a 20-km-long, narrow, winding estuary in northwest Peru, at ~6°S, is such a Holocene marine coastal evaporitic system (Morris and Dickey, 1959; Brantley et al., 1984). The observed stable lateral mineral zonation and the lack of bittern salts (potassium or magnesium salts) suggest a balance between surface influx of seawater evaporation and bottom flow removal of dense potassium and magnesium-rich brines (Brantley et al., 1984). The incursion of an ancient brine that evolved in the Salaverry Basin in middle to late Miocene, when the structural barrier between it and the neighboring western basins was subaerially exposed, was suggested by Suess, von Huene, et al. (1988). The lower-than-normal seawater $^{87}Sr/^{86}Sr$ ratios of the interstitial waters (Table 12) rule out the nonmarine origin and are strongly suggestive of a marine origin for the brine.

The chemical evolution of seawater during progressive evaporation has been studied extensively (e.g., Usiglio, 1849; Zherebtsova and Volkova, 1966; Braitsch, 1971; Holser, 1979a; Brantley et al., 1984; McCaffrey et al., 1987). In summary, Cl⁻ and Na⁺ concentrations increase conservatively until halite precipitation at 10 to 11 times seawater evaporation. K⁺ and Mg²⁺ concentrations increase conservatively up to ~70 times that of seawater evaporation. SO₄⁻ concentration increases nonconservatively to ~70 times evaporation, beyond which it starts to decrease sharply. Calcite (CaCO₃ and gypsum (CaSO₄ · 2H₂O) begin to precipitate at ~1.8 and ~3.8 times seawater concentrations, respectively, beyond which Ca²⁺ concentrations decrease sharply to practically zero at ~15 times evaporation. Sr²⁺ concentrations increase during carbonate precipitation, and similar to Ca²⁺, decrease strongly during gypsum or anhydrite precipitation and continue to decrease during halite precipitation (Zherebtsova and Volkova, 1966). After an initial increase, pH decreases with progressive evaporation, reaching values of 7.3 to 7.4 at the onset of halite precipitation (e.g., Brantley et al., 1984; McCaffrey et al., 1987). The density of the brine at this stage of evaporation is ~1.3. Thus, a marine brine within the halite facies should be enriched in Cl⁻, SO₄²⁻, Na⁺, K⁺, Mg²⁺, and depleted in Ca²⁺ and Sr²⁺ relative to seawater concentrations. As illustrated in Figures 2 through 11, the interstitial waters, although significantly enriched in Cl⁻, SO₄²⁻, Na⁺ and Mg²⁺, are also enriched in Ca²⁺ and Sr²⁺, but only slightly in K⁺ relative to seawater concentrations. Analysis of bromine,
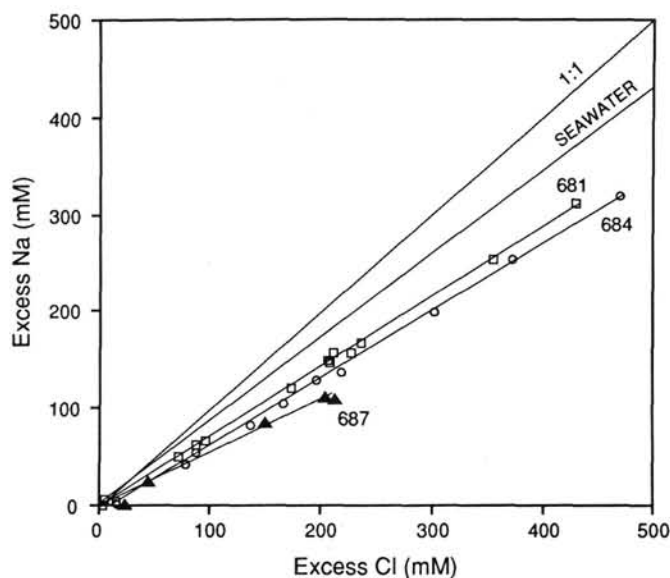
Figure 13. Plots of sodium in excess of seawater concentration vs. chloride in excess of seawater concentration in interstitial waters of Sites 681, 684, and 687. Lines of slope of Na⁺/Cl⁻ ratio of halite (1:1) and seawater are also shown.

which concentrates almost conservatively up to ~90 times that of seawater evaporation, is still in progress.

Cl⁻ and Na⁺ Profiles

The strong positive Na⁺ gradients with depth (Figs. 2–6) and the systematic decrease in the magnitude of the Na⁺/depth gradients from north to south correspond directly to those of chloride. Except for Site 686, the southernmost site (13°S with Na⁺ concentrations strongly influenced by ion exchange with NH₄⁺, the Na⁺/Cl⁻ ratios of all the shelf sites' interstitial waters (shown in Figure 13) have approximately similar gradients that are below a 1:1 value and below the seawater Na⁺/Cl⁻ ratio of ~0.85. This observation constrains the type of brine that is influencing the interstitial-water profiles. If the brine formed from halite dissolution, it would have a Na⁺/Cl⁻ ratio of 1:1. If the brine formed from evaporated seawater before halite precipitation, it would have the same Na⁺/Cl⁻ ratio as seawater. Because the Na⁺/Cl⁻ ratio of seawater is <1 and that of halite is 1:1, the behavior of Na⁺ and Cl⁻ differ during seawater evaporation within and beyond the halite facies; Cl⁻ remains nearly constant up to ~60 times evaporation, whereas Na⁺ decreases. Thus, halite precipitation will lower the Na⁺/Cl⁻ ratio of the residual brine, which is what was observed. Thus, the data may reflect flow of a residual brine formed by an evaporative process that has involved halite precipitation. At the Bocaña de Virrila, Peru, such a modern marine evaporitic system exists. Its chemistry suggests ~15 times seawater evaporation (Morris and Dickey, 1959; Brantley et al., 1984).

Possible origins of the observed systematic decrease in the magnitude of the Cl⁻ gradients, illustrated in Figure 12A, are (1) the brine exists directly beneath all the sites, at depths that systematically increase from north to south; or (2) the interstitial-water samples reflect a north-to-south sequence of increasing degrees of dilution of the brine with seawater or with diagenetically modified seawater.

From the beginning of halite precipitation, at 10 to 11 times seawater evaporation, until evaporation reaches ~60 times, the Cl⁻ remains nearly constant at 5600 to 5800 mM. Thus,

extrapolations of the essentially linear Cl^-/depth profiles (Fig. 12A) to this Cl^- value (assuming similar physical properties with depth) imply brine depths of approximately 1000 m at Sites 684 and 681, of ~1700 m at Site 680, and of >3 km at Sites 687 and 686. The large calculated brine depths for Sites 680, 687, and 686 are greater than basement depths derived from seismic-reflection profiles (von Huene, this volume) that rule out the first option. To evaluate the second option, the possibility of chemical mixing between the two end-members (brine and seawater) will be investigated.

Two End-Member Mixing System

Assuming no modifications by reactions or by other processes, the chemical and/or isotopic compositions of pairs of constituents in a mixed fluid derived by mixing of two end-member fluids can be correlated linearly as follows:

$$X_{iw} = fX_b + X_{sw} (1 - f), \quad (1)$$

$$Y_{iw} = fY_b + Y_{sw} (1 - f), \quad (2)$$

where X and Y represent concentrations of constituent pairs; the subscripts refer to the brine (b) and seawater (sw) end-members, and the interstitial water (iw); and f is the weight of fraction of $b/b+sw$. Thus,

$$Y_{iw} = X_{iw} \frac{Y_b - Y_{sw}}{X_b - X_{sw}} + \frac{Y_{sw}X_b - Y_bX_{sw}}{X_b - X_{sw}}. \quad (3)$$

This is a straight-line equation providing a linear correlation between the concentrations of component pairs, X and Y, in the mixed fluid. The equation, however, produces a hyperbolic mixing curve between the concentration of an ion and its isotopic composition; for example, between Sr^{2+} concentration (X_{iw}) and $^{87}Sr/^{86}Sr$ ratio (Y_{iw}). The equation can be easily transformed into a straight-line relationship by plotting Y vs. $1/X$, instead of Y vs. X.

Accordingly, plots of pairs of ions such as Na^+, K^+ or Mg^{2+} vs. Cl^- concentrations in marine-derived fluids should provide straight lines in interstitial waters of mixing systems, such as the one envisioned here, if they behave conservatively. As seen in Figures 13 and 14, each pair of ions behaves distinctly, however. The relationships between Na^+ and Cl^- are linear (Fig. 13), as predicted by the above equations. Except for Site 687, which clearly indicates mixing between three end-members, the plots of K^+/Cl^- of all the other saline shelf sites are practically linear (Fig. 14A). However, their slopes differ, as seen in Figure 12. Site 686, with the smallest Cl^- gradient, has the steepest K^+/Cl^- slope, indicating mixing between seawater and a second end-member fluid having high K^+ but low Cl^- concentrations. And the K^+/Cl^- slope of Site 681 (11°S), one of the two most saline sites, is essentially zero, indicating mixing between seawater and a second end-member fluid having seawater K^+ but high Cl^- concentrations. An even more complex situation is illustrated in Figure 14B, of plots of Mg^{2+} vs. Cl^-; none is linear as predicted. All the plots show mixing between three components. At first, at the lower concentration range, the mixing is between seawater and a second end-member fluid having lower Mg^{2+} and higher Cl^- concentrations. The mixing line then curves and connects to a second line influenced by mixing with another end-member fluid having high Mg^{2+} and Cl^- concentrations, possibly the original brine considered in the above two end-member mixing system.

Clearly, the brine has high Na^+, K^+ and Mg^{2+} concentrations, typical for a marine brine within the halite facies. The
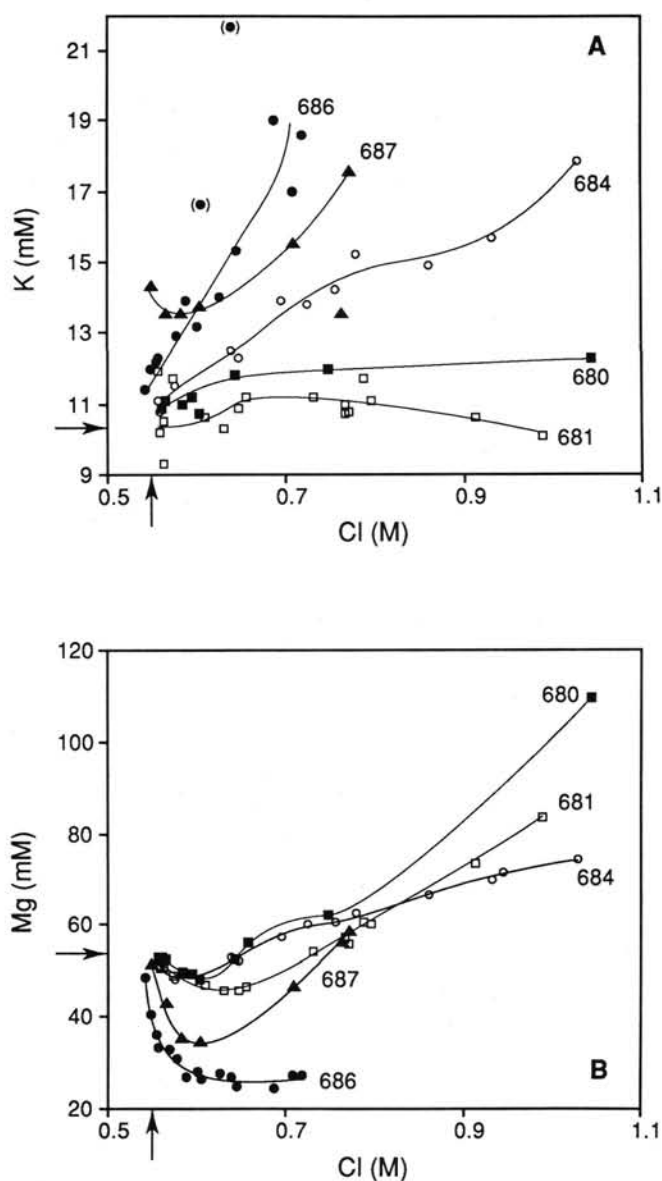
Figure 14. Plots of concentrations. A. Potassium. B. Magnesium vs. chloride in interstitial waters of shelf Sites 680, 681, 684, 686, and 687.
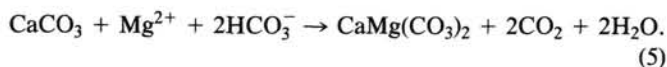
mixing relationships between the brine and seawater are complicated by diagenetic reactions, which significantly modified the K^+ and Mg^{2+} concentrations in the interstitial waters. Mixing between seawater and the modified interstitial water dominates the first segment of the plots (Fig. 14B), and mixing with the marine brine dominates the deeper stratigraphic sections at each of the sites. As expected from the distance to the brine source, the southernmost sites are more strongly influenced by the modified interstitial-water end-member, and the northern sites are primarily influenced by mixing between seawater and the brine.

The most important diagenetic reactions that modify the chemistry of interstitial waters in organic-rich sediments and saline systems are, for K^+, ion-exchange, adsorption-desorption, and silicates precipitation, e.g., K-rich clay minerals, K-feldspars, and K-zeolites (e.g., Sayles and Mangelsdorf, 1977; Carpenter, 1978; Eugster and Jones, 1979; Kastner, 1981). A strong positive correlation between K^+ and NH_4^+ concentrations was observed at all sites. Site 686, with the

highest NH_4^+ concentrations of up to 45 mM, has the highest K^+ concentration (~19 mM). Ion exchange between K^+ and NH_4^+ in organic-rich environments has been documented (Gieskes, 1973, 1975; Rosenfeld, 1977; Mackin and Aller, 1984). The nonstoichiometric relationships between sulfate reduction, alkalinity, phosphate and ammonia (Tables 2 to 6 and Figure 15), in particular the elevated alkalinity, phosphate, and ammonia concentrations at the southernmost Sites 686 and 687, strongly indicate increased dilution of the brine with an extensively modified interstitial-water end-member during its passage from north to south.

For Mg^{2+}, dolomite formation mainly by replacement of a $CaCO_3$ precursor but also by direct precipitation, is the most important diagenetic reaction that modifies marine-derived fluids. This reaction not only modifies the Mg^{2+}, Ca^{2+}, Sr^{2+}, and carbonate ion concentrations of the fluids, it often also significantly reduces the SO_4^{2-} concentration and influences the concentrations of several other minor ions, such as Fe^{2+} and Mn^{2+} (e.g., Shearman, 1963; Illing et al., 1965; Baker and Kastner, 1981; Garrison et al., 1984; Baker and Burns, 1985). The two dolomitization reactions of a $CaCO_3$ precursor, enhanced in diagenetic environments having active bacterial

$$2CaCO_3 + Mg^{2+} \rightarrow CaMg(CO_3)_2 + Ca^{2+}. \qquad (4)$$

$$CaCO_3 + Mg^{2+} + 2HCO_3^- \rightarrow CaMg(CO_3)_2 + 2CO_2 + 2H_2O. \qquad (5)$$

The first reaction, which liberates Ca^{2+}, then may react with SO_4^{2-} to form anhydrite.

$$2CaCO_3 + Mg^{2+} + SO_4^{2-} \rightarrow CaMg(CO_3)_2 + CaSO_4. \qquad (6)$$
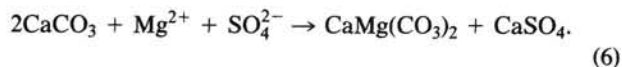
Some dolomite may also directly precipitate from the interstitial water, as

$$Ca^{2+} + Mg^{2+} + 4HCO_3^- \rightarrow CaMg(CO_3)_2 + 2CO_2 + 2H_2O. \qquad (7)$$
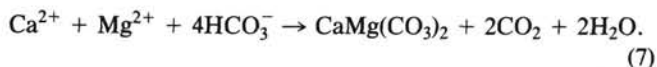
Ion-exchange and adsorption-desorption reactions involving Mg^{2+}, as well as complexation with sulfate and carbonate, likewise modify the chemistry of marine fluids (Millero, 1974; Millero and Schreiber, 1982; Bischoff et al., 1975; Sayles and Mangelsdorf, 1977; von Breymann et al.; Suess, von Huene, et al., this volume).

Ca^{2+}, Mg^{2+}, and Sr^{2+} Profiles

Within the halite facies, an unmodified marine brine has higher Mg^{2+}/Cl^- and lower Ca^{2+}/Cl^- and Sr^{2+}/Cl^- ratios than seawater. The depth profiles of these ratios are shown in Figures 16A, 16B, and 16C, respectively. These more complicated profiles do not simply reflect the decreasing influence of the brine with increasing dilution from north to south, they also are modified by diagenetic reactions, especially carbonateformation. The Mg^{2+}/Cl^- and Ca^{2+}/Cl^- depth profiles show two main features: (1) in the upper portions (0–40 m) they decrease with depth and the profiles then curve, and (2) in the lower portions, except for Mg^{2+}/Cl^- at Sites 684 and 686, they increase almost linearly with depth. The magnitude of the depth gradient of the latter portions decreases generally from north to south.

Considering first the data in the shallow-depth portion, the decreases in Mg^{2+}/Cl^- may reflect dolomitization by the above
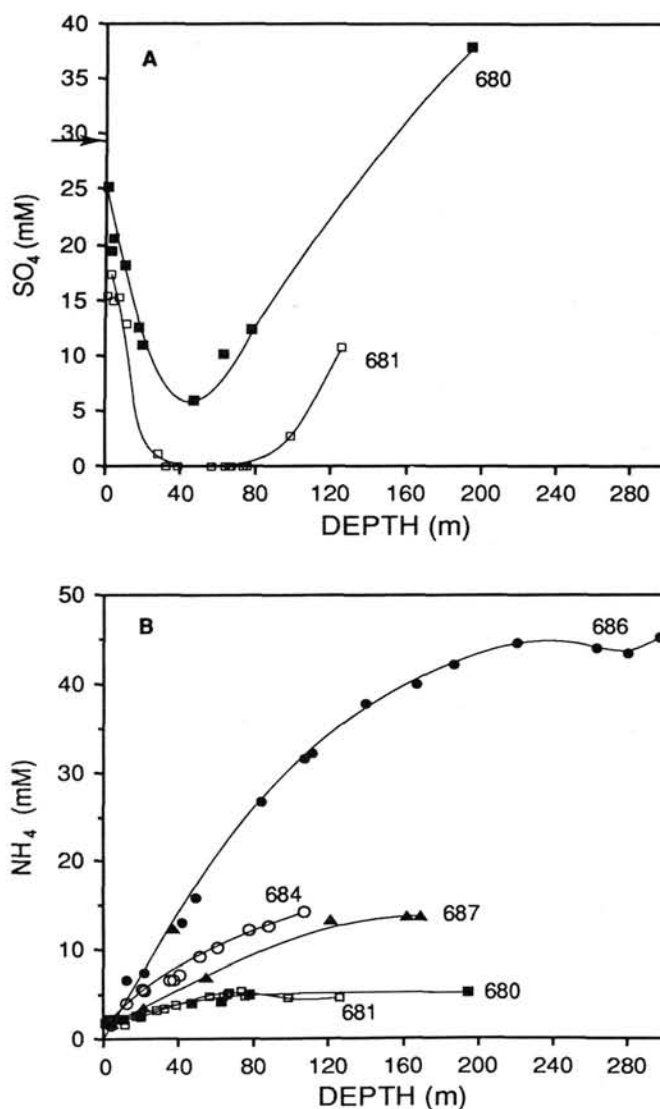

Figure 15. Depth profiles in interstitial waters of concentrations. A. Sulfate for Sites 680 and 681. B. Ammonia for shelf Sites 680, 681, 684, 686, and 687.

Equations 4 and/or 5. However, Equation 4 would increase the Ca^{2+}/Cl^- ratio in the interstitial water, and Equation 5 would maintain it at a constant ratio. The observed decrease in the Ca^{2+}/Cl^- ratio thus reflects calcite precipitation, which is supported by the strong maxima seen in the depth profiles of Mg^{2+}/Ca^{2+} ratio shown in Figure 16D. The linear increases in the Mg^{2+}/Cl^- ratios below ~40 mbsf do not simply reflect different degrees of mixing with the subsurface Mg^{2+}/Cl^- enriched brine; the corresponding linear increases in the Ca^{2+}/Cl^- ratios and decreases in the Mg^{2+}/Ca^{2+} ratios indicate continued dolomitization at depth or mixing with an end-member fluid that has been influenced by dolomitization. At depth, at Site 684, dolomitization is apparently so intense that even in the deeper portion of the Mg^{2+}/Cl^- profile the ratio continues to decrease with depth, in accordance with the Ca^{2+}/Cl^- gradient, which is the steepest one among all saline shelf sites and with the lowest observed Mg^{2+}/Ca^{2+} ratio of 2.6 at ~100 mbsf.

Another method by which the influence of reactions in the carbonate system on interstitial-water chemistry can be eval-
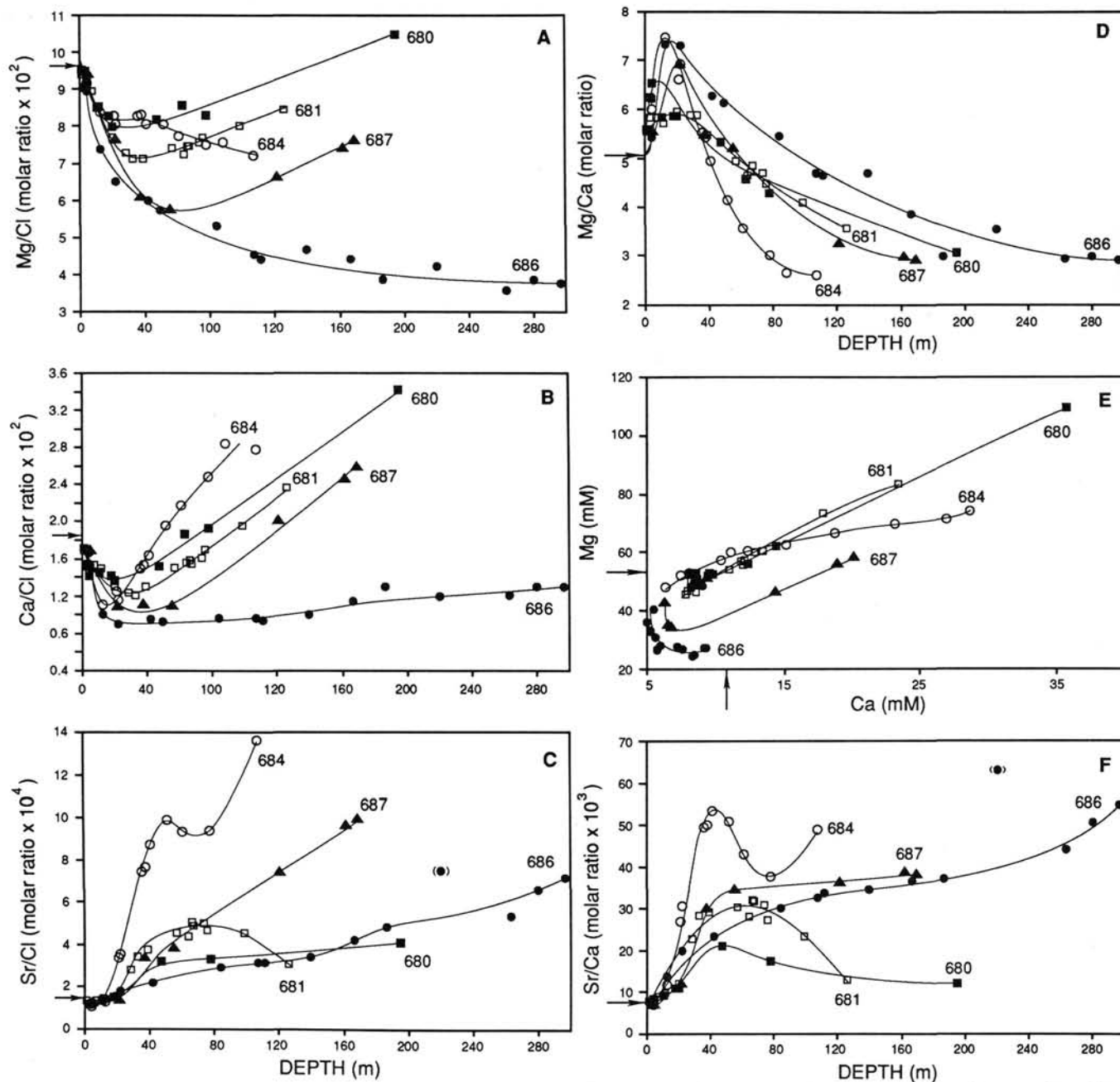
Figure 16. Depth profiles in interstitial waters of molar ratios. A. Mg^{2+}/Cl^-. B. Ca^{2+}/Cl^-. C. Sr^{2+}/Cl^-. D. Mg^{2+}/Ca^{2+}. F. Sr^{2+}/Ca^{2+}. E. Magnesium vs. calcium concentrations. (For Sites 680, 681, 684, 686 and 687.)

uated is through the use of plots of Ca^{2+}, Mg^{2+}, and Sr^{2+} concentrations vs. depth in conjunction with plots of Mg^{2+} vs. Ca^{2+} and/or Sr^{2+}/Ca^{2+} and Sr^{2+}/Cl^- ratios vs. depth (Figs. 16E, 16F, and 16C). Residual marine fluids modified by carbonate diagenesis may be characterized by the direction and magnitude of the gradients of these depth profiles. Each reaction produces a unique combination of profiles, shown in Table 13.

The Mg^{2+}/Ca^{2+} profiles of all shelf sites rapidly and sharply increase with depth, reaching maxima between 5 and 15 mbsf. Below this depth, the Mg^{2+}/Ca^{2+} ratios decrease with depth in the following sequence of sites:

$$684 > 687 > 680 \approx 681 > 686.$$

Similarly, all Sr^{2+}/Ca^{2+} depth profiles show marked increases in the uppermost ~40 mbsf. At greater depths, they

differ considerably from the Mg^{2+}/Ca^{2+} profiles. At Sites 686 and 687 (13°S), the Sr^{2+}/Ca^{2+} ratios continue to increase with depth; at Site 684 (9°S), after a short but steep excursion toward lower Sr^{2+}/Ca^{2+} ratios, the plot curves back, and the ratios then continue to increase with depth. Only at Sites 680 and 681 (11°S) were decreases in the Sr^{2+}/Ca^{2+} ratios with depth seen. Moreover, only at three of the sites, 680, 681 and 684, were Sr^{2+}/Ca^{2+} maxima observed. These maxima occur directly beneath the Mg^{2+}/Ca^{2+} maxima (Figs. 16F and 16D). At depths of >80 mbsf, the Sr^{2+}/Ca^{2+} ratios in the interstitial waters decrease in the following order of sites:

$$684 > 687 > 686 > 681 > 680.$$

This sequence, which is considerably different from the one for Mg^{2+}/Ca^{2+}, is consistent with the distinctive behavior

Table 13. Characterization of the Mg^{2+}/Ca^{2+} and Sr^{2+}/Ca^{2+} ratios and of the Ca^{2+}, Mg^{2+}, and Sr^{2+} concentrations of marine interstitial waters modified by carbonate crystallization or dissolution.

Reaction	Mg^{2+}/Ca^{2+}	Sr^{2+}/Ca^{2+}	Ca^{2+}	Mg^{2+}	Sr^{2+}
Calcite precipitation	Increases considerably	Increases moderately	Decreases	Constant	Decreases
Dolomitization reaction 1 (Eq. 5)	Decreases considerably	Decreases moderately	Increases	Decreases	Increases
Dolomitization reaction 2 (Eq. 6)	Decreases moderately	Increases	Constant	Decreases	Increases
Dolomite precipitation, reaction 3 (Eq. 7)	Increases considerably	Increases considerably	Decreases	Decreases	Decreases
Calcite dissolution	Decreases considerably	Decreases moderately	Increases	Constant	Increases
Dolomite dissolution	Decreases moderately	Decreases moderately	Increases	Increases	Increases

of these two ionic ratios during carbonate diagenesis, summarized in Table 13. Accordingly, much of the observed marked increases in the Sr^{2+}/Ca^{2+} ratios in the uppermost 30 to 40 mbsf are generated by calcite precipitation. The maxima of Sr^{2+}/Ca^{2+} ratios are, however, within the depth zone of accelerated dolomitization by Equation 6, the zone of intense sulfate reduction and bicarbonate production. The compounded effect of high Mg^{2+}/Ca^{2+}, low SO_4^{2-} and high bicarbonate on dolomitization (e.g., Lippman, 1973; Baker and Kastner, 1981; Baker and Burns, 1985; Kastner and Anderson, unpubl. data), is most intense at the depth of the

Mg^{2+}/Ca^{2+} maximum, which is the depth of the onset of rapid dolomitization.

The deeper portions of the Sr^{2+}/Ca^{2+} and Mg^{2+}/Ca^{2+} profiles at Sites 684, 686, and 687 are consistent with ample dolomitization, primarily by Equation 6, as may be expected within the carbonate reduction (methanogenesis) zone. At Sites 681 and particularly at Site 680, however, the subsurface brine also exerts its control on the SO_4^{2-} composition of the interstitial waters (Fig. 15). In the portions of elevated SO_4^{2-} concentrations beneath the minima, the Sr^{2+}/Cl^- ratios barely increase with depth and the Sr^{2+}/Ca^{2+} gradients, although
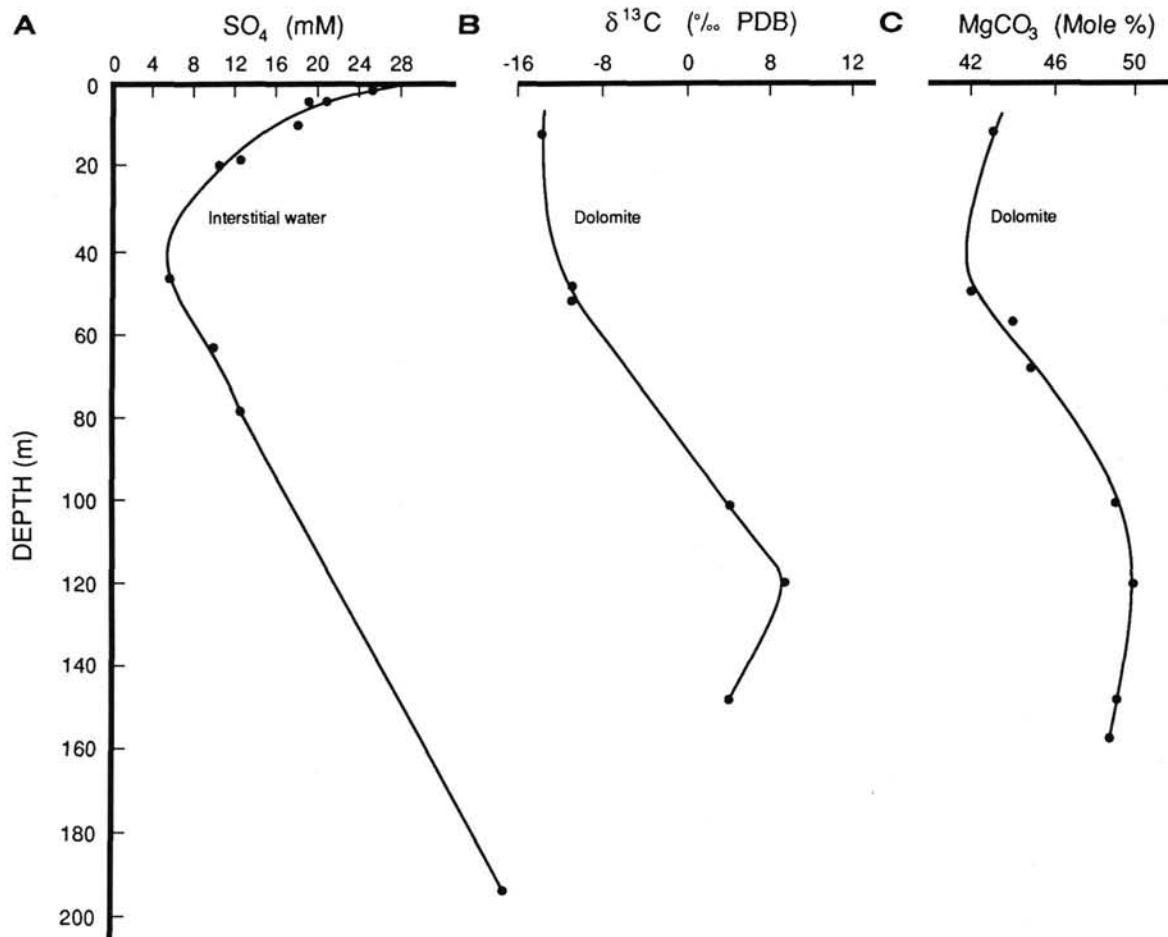

Figure 17. Depth profiles for shelf Site 680. A. Sulfate concentrations in interstitial waters. B. $\delta^{13}C$. C. Mole% $MgCO_3$, in separated dolomites.

gentle, decrease with depth. The corresponding decreases in the Mg^{2+}/Ca^{2+} depth profiles are consistent with the interpretation of either minor dolomitization by Equation 5, or mixing with a brine end-member diagenetically modified by the same reaction, but with no local active dolomitization. The latter option points to an end-member having Mg^{2+}/Ca^{2+} and Sr^{2+}/Ca^{2+} ratios lower than, and having SO_4^{2-} concentrations higher than, the observed values at these two sites.

The plots in Figure 17 support the above second option, suggesting that at Site 680 the incursion of SO_4^{2-} from below, from the subsurface brine, considerably reduced or probably stopped dolomitization below ~60 mbsf. Hence, the $\delta^{13}C$ values of the dolomites at this site (Fig. 17) do not reflect the modern interstitial-water chemistry. The deeper, more stoichiometric, dolomites having heavy $\delta^{13}C$ values indicate formation within a methane-rich environment, which has disappeared because of the incursion of SO_4^{2-} from the subsurface brine. Fortunately, the primary interstitial-water chemical system left its impression within the dolomites; these must have formed early. The modern interstitial waters at this site contain very low concentrations of CH_4 <150 $\mu L/L$ (Kvenvolden, this volume).

Strontium Isotope Ratios

Depth profiles of $^{87}Sr/^{86}Sr$ ratios for the interstitial waters of the saline shelf sites are illustrated in Figure 18, where they have been separated into two groups because of some additional complexities associated with the profiles for Sites 680 and 686.

Sites 681, 684, and 687

Figure 18A presents the profiles for Sites 681, 684, and 687. All are characterized by large decreases in $^{87}Sr/^{86}Sr$ ratios with increasing depth, with, for Site 684, a small increase in the lowermost sample. Such changes cannot be attributed to changes in the strontium isotopic composition of modern interstitial seawaters, the $^{87}Sr/^{86}Sr$ ratio of seawater having increased with time, because the observed changes are much too large. The oldest sediments from which interstitial waters were recovered at each of these sites are ca. 5 Ma (Site 681), ca. 15 Ma (Site 684), and ca. 2 Ma (Site 687), and the $^{87}Sr/^{86}Sr$ ratios of seawaters of these ages are approximately 0.7090, 0.7088, and 0.7091 (see Elderfield, 1986). In comparison, the minimum values at each site are ~0.7083, 0.7082 and 0.7088, respectively. The comparison of interstitial-water $^{87}Sr/^{86}Sr$ ratios with ratios of seawater of the age of coexisting sediment is complicated by upward diffusion of strontium from older strata (Elderfield and Gieskes, 1982; Gieskes et al., 1986). The decreases in $^{87}Sr/^{86}Sr$ ratios with depth are associated, however, with increases in Sr^{2+} concentrations (Table 12). Therefore, an additional source (or sources) of strontium is required.

The association of decreasing strontium isotopic compositions with increasing Sr^{2+} concentrations in interstitial waters is a common phenomenon for ocean drilling sites and has been attributed to processes of volcanic matter alteration and carbonate recrystallization (Elderfield and Gieskes, 1982). However, in this case, it may be significant that such low strontium isotope ratios were not found in interstitial waters from the slope sites at equivalent depths (Table 12). Moreover, the magnitudes of the depth gradients of strontium isotope ratios correspond qualitatively to those of chloride. The chloride gradients, ranked according to site (Fig. 12A), follow the sequence:

$$684 > 681 > 680 > 687 > 686,$$

which is the same as that for $^{87}Sr/^{86}Sr$ ratios, except for Site 680, which is complicated by values higher than for modern seawater and will be discussed later. We mentioned earlier that such gradients appear to be diffusive profiles between seawater and a
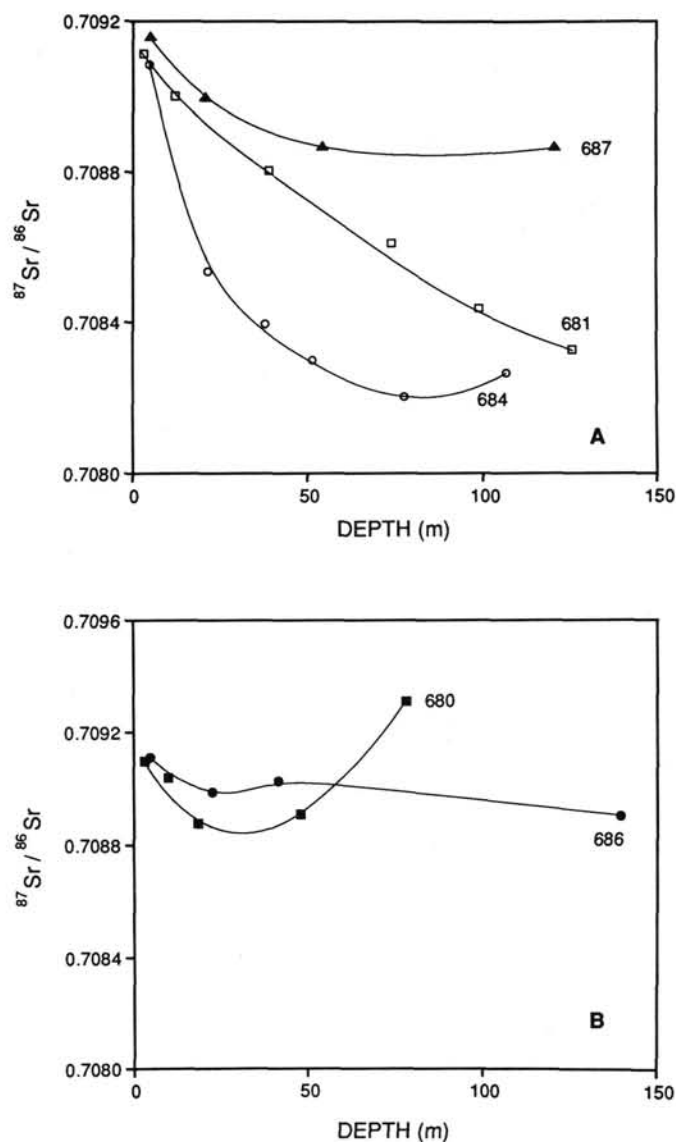

Figure 18. Depth profiles of $^{87}Sr/^{86}Sr$ ratios of interstitial waters for shelf sites. A. Sites 681, 684, and 687. B. Sites 680 and 686.

subsurface brine located at depths below the holes. As discussed and shown below, the assumption that the profiles simply reflect a deep saline source mixing with seawater is oversimplistic. It is important to emphasize, however, that the source of the high-chloride fluids was never sampled.

Thus, the presence of the subsurface brine appears not only to exert a control on the major cations, but also on the strontium isotopic ratios of the interstitial waters. This fact can be used to further constrain the origins of the brine. As already discussed, the low $^{87}Sr/^{86}Sr$ ratios of the interstitial waters rule out the option of a meteoric water- or continental-derived dense brine.

One approach by which the origin of the brine may be evaluated is through the use of plots of $^{87}Sr/^{86}Sr$ ratios vs. Cl^- concentrations (Fig. 19). Consider first the data for Site 684, which show a hyperbolic relationship with the $^{87}Sr/^{86}Sr$ ratios trending to a near constant value of approximately 0.7082 with increasing chloride concentrations. A conservative mixing line between these two parameters will only be linear for a system with two end-members, each with the same Sr^{2+}/Cl^-

ratio. A concave curve, as shown for Site 684, must indicate a higher Sr^{2+}/Cl^- ratio for the brine end-member at this site than for seawater, if this representation of the mixing relationship is correct. This result is fortunate because it enables the strontium isotopic composition of the end-member to be defined, despite its dilution by normal seawater. The end-member ratio of 0.7082 is equivalent to a value of ca. 22-Ma-old seawater and indicates an early Miocene age for the brine at this site. This interpretation is consistent with the hypothesis of incursion of an ancient dense marine brine, but is not consistent with a middle to early Miocene age brine.

In detail, the form of Figure 18A for this site indicates an increase in $^{87}Sr/^{86}Sr$ ratio in the deepest sample analyzed, which is not consistent with this simple picture of two end-member mixing. A further difficulty with this interpretation is that a concave mixing curve for $^{87}Sr/^{86}Sr$ vs. Cl^- is only seen for Site 684 (Fig. 19). For example, the deeper part of the curve for Site 681 is slightly convex. Furthermore, as noted above, the shape of the curve for Site 684 implies that the brine end-member is characterized by a high strontium concentration, which is unlikely for a marine brine within the halite facies (Zherebtsova and Volkova, 1966). The explanation for this would seem to be that there is an additional source of Sr^{2+} at the base of Site 684. It is also associated with a rapid increase in Sr^{2+}/Cl^- ratio in the deepest sample (Fig. 16C). Thus, there is a further source that has had little effect on the $^{87}Sr/^{86}Sr$ ratio, but has led to a large increase in Sr^{2+} concentration. It seems probable that this is the result of intense dolomitization.

Figure 18A presents the profiles for Site 684, the farthest north (9°S), and for Site 687, the farthest south (13°S). The strontium isotope vs. chloride plot for this site also seems to be convex, but approaches a higher end-member $^{87}Sr/^{86}Sr$ ratio of approximately 0.7089, equivalent to ca. 12-Ma-old seawater. This younger "age" is consistent with the chemical gradients in the interstitial waters. The sequence of Cl^- and $^{87}Sr/^{86}Sr$ gradients indicated above decreases from north to south along the shelf, making Site 684 nearest the source of the brine and Site 687 farthest from the source. Thus, each almost end-member is itself part of a mixing relationship, as the brine flows in a southerly direction and is progressively diluted with normal modern seawater or with interstitial waters.

This explanation is further complicated by data for Site 681 from 11°S, intermediate between the locations of Sites 684 and 687. These data (Fig. 19) are not clear cut, but do appear to show a near-linear mixing relationship, pointing to an end-member ratio that is lower than the Site 684 value. Moreover, if the mixing model is correct, the more-linear mixing relationship for this site must mean that the brine end-member at Site 681 has a lower Sr^{2+}/Cl^- ratio than at Sites 684 and 687. It is probable that the hydrology is complex and is inadequately represented by only three drill sites. Nevertheless, such difficulties in interpretation would seem to indicate that the two end-member model describes the mixing relationships to a first approximation only.

The second approach by which the origin of the brine may be evaluated is through the combined use of strontium isotopes and concentrations. For two end-member mixing between brine (b) and seawater (sw), the relationship between the Sr^{2+} concentration in the interstitial water (Sr_{iw}) and its $^{87}Sr/^{86}Sr$ ratio (Y_{iw}) is given by

$$Y_{iw} = \frac{Sr_b \cdot Sr_{sw}(Y_{sw} - Y_b)}{Sr_b - Sr_{sw}} \cdot \frac{1}{Sr_{iw}}$$
$$+ \frac{Sr_b \cdot Y_b - Sr_{sw} \cdot Y_{sw}}{Sr_b - Sr_{sw}} \quad (8)$$

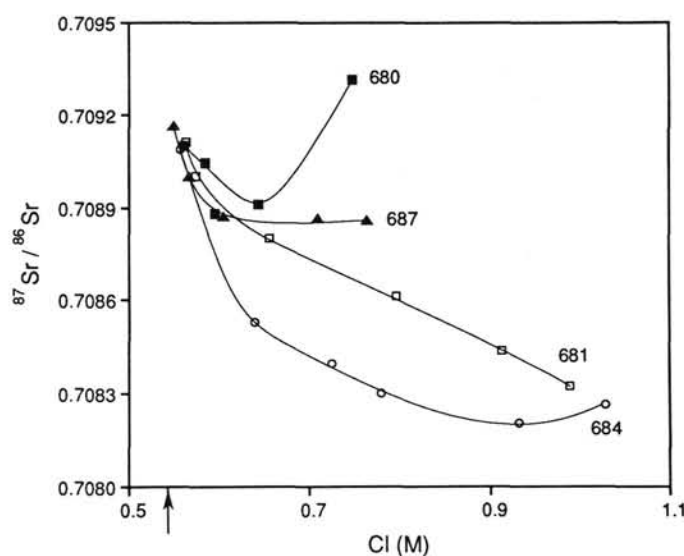
Figure 19. Plots of $^{87}Sr/^{86}Sr$ ratios vs. chloride concentrations in interstitial waters of Sites 680, 681, 684 and 687.
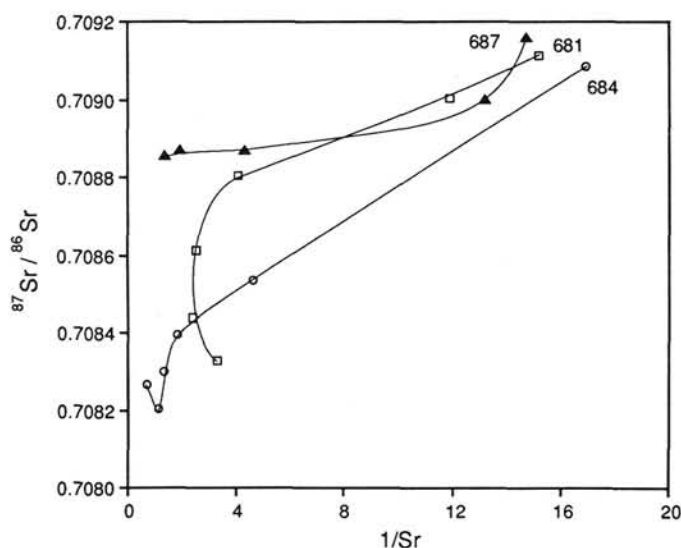

Figure 20. Plots of $^{87}Sr/^{86}Sr$ ratios vs. 1/strontium concentrations in interstitial waters of Sites 681, 684, and 687.

Plots of $^{87}Sr/^{86}Sr$ ratio vs. $1/Sr^{2+}$ are illustrated in Figure 20. These plots are not linear, as predicted by the above equation, and must indicate a more complex mixing regime than was assumed when the Cl^- data were used (Fig. 19). All profiles indicate mixing between three end-members. Consider first the data for Site 681, the intermediate of the three sites under discussion. The plot in Figure 20 shows two main features. At low Sr^{2+} concentrations (high $1/Sr^{2+}$ ratios), the plot shows a near-linear portion, indicating mixing between seawater (end-member) and a second end-member having a low $^{87}Sr/^{86}Sr$ ratio and a high Sr^{2+} concentration. This mixing line then curves toward a second line, indicating mixing with a third end-member having an even lower $^{87}Sr/^{86}Sr$ ratio but a low Sr^{2+} concentration. A similar situation can be seen for Site 684 (Fig. 20). There is a linear portion linking seawater composition to a low $^{87}Sr/^{86}Sr$ ratio and high Sr^{2+} concentration end-member that is modified by a third end-member, again of low $^{87}Sr/^{86}Sr$ ratio and low Sr^{2+} concentration. The plot for Site 687 in Figure 20 does not show the influence of the third end-member and is linear, except for the most shallow sample.

These results may be interpreted in terms of the effect of the subsurface brine upon the type of $^{87}Sr/^{86}Sr-Sr^{2+}$ relationship typical of interstitial waters. Without the influence of the brine, a distribution typified by a small decrease in $^{87}Sr/^{86}Sr$ ratio but a large increase in Sr^{2+} concentration would be expected (i.e., in Elderfield and Gieskes, 1982), and this is the reason for the mixing relationship between the first two end-members described above. Superimposed upon this relationship is the effect of the brine, the third end-member, which is characterized by a low $^{87}Sr/^{86}Sr$ ratio and, importantly, a low Sr^{2+} concentration (i.e., a high $1/Sr^{2+}$ ratio). Thus, the sequence of sites is consistent with the decreasing influence of the brine from north to south.

It is clear from this approach that the brine itself must have a lower $^{87}Sr/^{86}Sr$ ratio than the lowest value recorded for the interstitial waters. Therefore, the early Miocene age must be regarded as a maximum age, and the seawater that constitutes the brine might be of an even earlier age. Another factor of importance is that the brine is characterized by a low Sr^{2+} concentration, as expected from a seawater-derived brine within the halite facies (Zherebtsova and Volkova, 1966). The same conclusion was obtained independently from the earlier synthesis of the major constituents data, especially from the Sr^{2+}/Cl^- depth profiles of Sites 680 and 681 (Fig. 16C).

Sites 680 and 686

The depth profiles of $^{87}Sr/^{86}Sr$ ratios for these sites are illustrated in Figure 18B. Although the sites are characterized by chloride enrichments (the highest recorded value of all sites was found at the base of Site 680), the profiles show an additional complexity not seen for the sites discussed above. In both, the decrease in strontium isotopic composition with depth is truncated at ~20 mbsf, below which the values level out (Site 686) or increase significantly (Site 680). The $^{87}Sr/^{86}Sr$ ratio in the lowermost sample from Site 680 is 0.70931, higher than the value for modern seawater. Clearly, an additional source is present here. The very high chloride concentrations for Site 680 (up to 1.04 mol) show that the brine forms a significant part of the interstitial fluids at this site, yet the strontium isotopic imprint of the brine (its low $^{87}Sr/^{86}Sr$ ratio) is not recognizable. This relationship supports the contention that the brine has a low Sr^{2+} concentration, which at Site 680 is swamped by the more radiogenic source of high strontium content. The origin of such postulated radiogenic strontium is uncertain at present. Sediments from Site 680 have not yet been analyzed, but sediments from other Leg 112 sites all have $^{87}Sr/^{86}Sr$ ratios below 0.7092 (see later). Influence by meteoric water is possible, although the high interstitial chloride values constrain the proportion that may be present. Except for one sample, oxygen and hydrogen isotopes of the interstitial waters of these two sites have not yet been analyzed.

Oxygen and Hydrogen Isotope Ratios

Oxygen and hydrogen isotope ratios of just 11 interstitial water samples, from four of the five saline shelf sites, have as yet been analyzed. The values range, for oxygen isotopes, from −1.90‰ to +0.3‰ and for hydrogen isotopes, from −17.60‰ to +5.60‰ (SMOW) (Table 14). A comprehensive analysis of such a small set of data therefore is unwarranted, particularly in this complicated hydrogeochemical system. Even the highest Cl^- concentration in an interstitial-water sample from the bottom of Site 680, of 1.04 M, reflects a significant degree of dilution of a marine brine that originated within the halite facies, with Cl^- concentrations of about 5.6 to 5.8 M. The $\delta^{18}O$ value of such an undiluted brine should be ~3 ±1‰ (SMOW)(e.g., Craig and Gordon, 1965; Lloyd, 1966; Holser, 1979b). In a conservative two end-member mixing system between brine and seawater, the expected $\delta^{18}O$ value of the above least diluted interstitial-water sample at Site 680 would be +0.03‰ to +0.04‰ values, easily overprinted by the complications of the system at this shelf.

Table 14. Oxygen and hydrogen isotopic composition of interstitial waters (‰ SMOW), Leg 112.

Core, section	Depth (mbsf)	$\delta^{18}O$	δD	Comments
112-680B-9H-4	77.9	−0.52	5.60	1
681B-1H-2	3.0	−0.08	−0.05	1
681C-5H-3	38.9	0.30	—	1
681B-12X-3	98.9	—	−5.56	1
681B-15X-1	126.0	−0.17	4.41	1
682A-34X-2	307.5	—	1.80	1 Contaminated by 13.8% SW
683A-9H-4	73.2	−0.20	5.05	1 Contaminated by 10.5% SW
683A-15X-1	127.1	−0.65	4.30	1 Contaminated by 7.2% SW
683B-3X-2	424.4	−1.38	−2.38	1
683B-6X-2	452.0	−0.58	−9.77	1
684B-3H-3	21.5	−0.20	−1.20	2
684C-8X-2	60.4	0.00	−4.50	2
684C-13X-1	106.9	—	−7.63	1
687B-3H-4	20.6	0.04	−0.19	1
687B-15X-1	120.7	−1.13	−12.90	1
687B-19X-1	169.0	−1.90	−17.60	2
688E-3R-4	365.0	−1.20	−8.50	2
Clathrate Samples				
685A-18X-8	165.6	—	19.30	1 Contains 51.4 mM Cl^-
688A-15X-7A	141.0	1.80	17.60	1 Contains 90.6 mM Cl^-

1 Analyzed by J. Welhan, σ D/H = 0.80; σ 0–18 = 0.12.
2 Analyzed by S. Epstein, δD ± 1‰; $\delta^{18}O$ ± 0.1.
SW = seawater.

Summary of Saline Shelf Sites

The chemistry of major ions and the strontium isotopic composition of the interstitial waters provide insight into the origin of the subsurface brine that profoundly influences the chemistry and diagenesis of the shelf environment of the Peruvian continental margin. These data indicate that the brine has a marine origin, and the $^{87}Sr/^{86}Sr$ ratios suggest an early Miocene "age" for the brine. The brine formed by evaporation of seawater within the halite facies. Carbonate and silicate diagenesis, ion-exchange, and adsorption-desorption reactions modified the chemistry and isotopic composition of the subsurface brine. Site 684 (9°S) must be nearest to the source of the brine, which becomes more diluted with seawater as it flows southward toward Site 686 (13°S) and beyond. Assuming an average constant flow rate at a depth of 500 to 700 mbsf, arrival at Sites 686 and 687 5 to 10 Ma, and Cl^- diffusion coefficients of 10^{-6} cm^2/s, the calculated average flow rate since early Miocene (~24 Ma is 3 to 4 cm/yr).

SITE 679

Site 679 is located at the seaward edge of the outer shelf, west of a structural ridge that separates it from the Salaverry Basin to the east (Fig. 1). Because of the special tectonic setting, the site is geochemically distinct, characterized by seawater Cl^- concentrations to ~200 mbsf and below in the middle Miocene section by significantly lower Cl^- concentrations (Figs. 7 and 12B). The deepest sample analyzed has 62% of seawater chloride. The structural ridge thus separates this site from the influence of the subsurface brine. Dilution with middle to late Miocene fresh water while the ridge was subaerially exposed, restricting the Salaverry Basin in which the brine evolved and acting as a recharge zone for fresh water into the seaward sequence, was proposed by Suess, von Huene, et al. (1988). The possibility of a considerably younger or even Holocene land-derived source of fresh water and subsurface flow within the sandy-silty Miocene horizon is not implicit in the $^{87}Sr/^{86}Sr$ ratios depth profile.

The $^{87}Sr/^{86}Sr$ ratio of seawater contemporaneous with the oldest sediments from which interstitial waters were recovered at this site, of ca. 15 Ma, is approximately 0.7088 (Elderfield, 1986). The lowest ratio determined at this site is
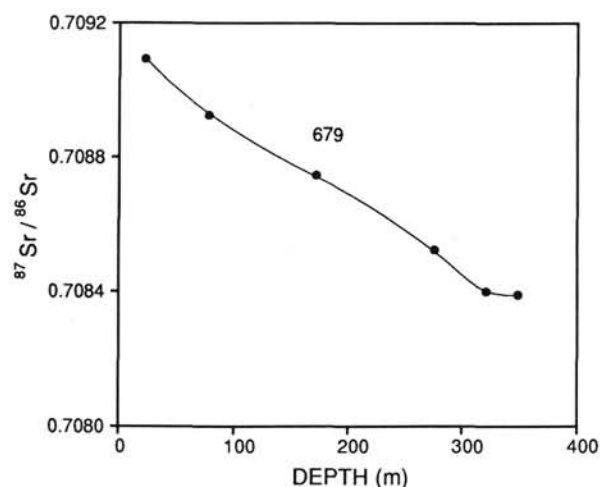
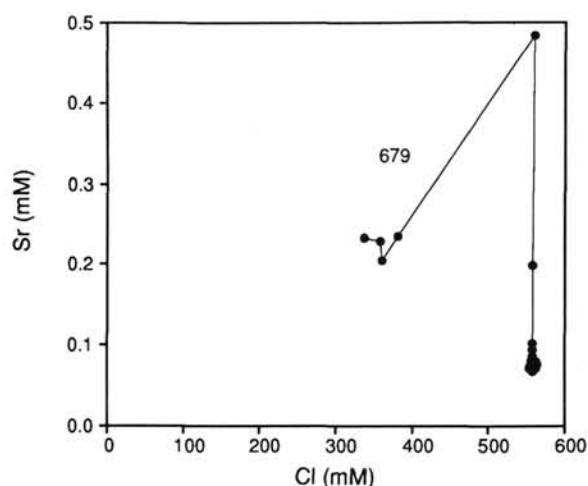Figure 21. Depth profile of $^{87}Sr/^{86}Sr$ of interstitial waters for Site 679.

Figure 22. Plots of $^{87}Sr/^{86}Sr$ ratios vs. chloride concentrations in interstitial waters of Site 679.

Figure 23. Plots of $^{87}Sr/^{86}Sr$ ratios vs. 1/strontium concentrations in interstitial waters of Site 679.

The Cl^- and Na^+ depth profiles illustrated in Figure 7 do not appear to be simple diffusion profiles; they show an additional complexity in that they are truncated at ~200 mbsf. A disturbance in the depth profile introduced by incursion of fresh water at 200 to 300 mbsf should have disappeared in >5 Ma, assuming approximately constant physical properties with depth. The depth profiles of alkalinity, ammonia, Ca^{2+}, and Sr^{2+} display maxima, and of Mg^{2+}/Ca^{2+} a minimum, at the depth of truncation of Cl^- and Na^+ (Fig. 7), suggesting an intensely active diagenetic front of carbonate reactions. This front may act as a diffusional barrier for Cl^- and Na^+. It occurs at a noticeable change in lithology at ~225 mbsf, at a major unconformity between the middle to late Miocene. A calcite-cemented section exists near the top of the boundary. These were clearly recorded in the bulk density, acoustic velocity, neutron porosity, and resistivity logs (Suess, von Huene, et al., 1988, Site 679 summaries). Porosities, for example, decrease from 80% to 70% above 80 to 90 mbsf through a transition zone between 80 and ≥200 mbsf having porosities of 70%, to 35% to 45% porosities at >275 mbsf.

The Ca^{2+}, Mg^{2+}, Sr^{2+}, and alkalinity depth profiles show further complexities (Fig. 7), all diagenetic in origin. Three distinct zones of carbonate diagenesis, which modify these as well as the Mg^{2+}/Ca^{2+}, Sr^{2+}/Ca^{2+}, and Mg^{2+}/Cl^- depth profiles (Figs. 24A, 24B, 24C), may be recognized. In the shallowest zone, between 0 to ~150 mbsf, these profiles have been modified by minor dolomitization by Equation 5 reaction (Table 15). The zone in the vicinity of the unconformity (~150 to ~230 mbsf) is marked by more intense dolomitization, by both dolomite reactions (Eqs. 5 and 6); this result is even reflected in the double truncation (small decrease) of the alkalinity depth profile, indicating dolomitization by reaction 2 (Eq. 5, Fig. 24D). Note that at the upper boundary of this zone, at ~150 mbsf, SO_4^{2-} reaches zero concentration. The deepest portion of the profiles below ~230 mbsf is characterized by combined dilution and dolomite formation by reaction 2 (Eq. 6, Table 15). The Na^+/Cl^- depth profile (Fig. 7) is modified by ion exchange with NH_4^+.

THE SLOPE SITES

The deep-water slope and accretionary complex sediments at the Peru continental margin are characterized by high

0.7084, the ratio of ~21-Ma-old seawater (Elderfield, 1986) (Table 12). This apparent discordance between the "ages" is not surprising in view of the relationship between the $^{87}Sr/^{86}Sr$ ratios and Sr^{2+} concentrations suggesting a multimixing system, as discussed above. Unlike the Cl^- depth profile, the $^{87}Sr/^{86}Sr$ ratios regularly decrease with depth (Fig. 21). The process responsible for this $^{87}Sr/^{86}Sr$ depth profile appears to be decoupled from the one responsible for the Cl^- profile. The influence by the low Cl^- layer is, however, apparent from the Sr^{2+} and other major ion concentration data (Table 7 and Fig. 7), which show dilutions in the low Cl^- zone. The low Sr^{2+}, Ca^{2+}, and Mg^{2+} values cannot, however, be simply explained by dilution with fresh water. For example, in Figure 22, which is a plot of Sr^{2+} vs. Cl^- concentrations, dissolved strontium concentrations increase with depth until the low chloride zone is reached, where these concentrations decrease to a minimum value of about 0.2 mM, and then increase slightly. The mixing line in the low-chloride portion of the plot does not extrapolate to a zero chloride end-member and suggests a complex mixing regime. A three end-member system is seen in Figure 23, where gradually decreasing strontium isotopic composition with depth is modified by the low-chloride, low-strontium zone having a much lower $^{87}Sr/^{86}Sr$ ratio. The low Cl^- interstitial waters have not yet been analyzed for oxygen and hydrogen isotopes.
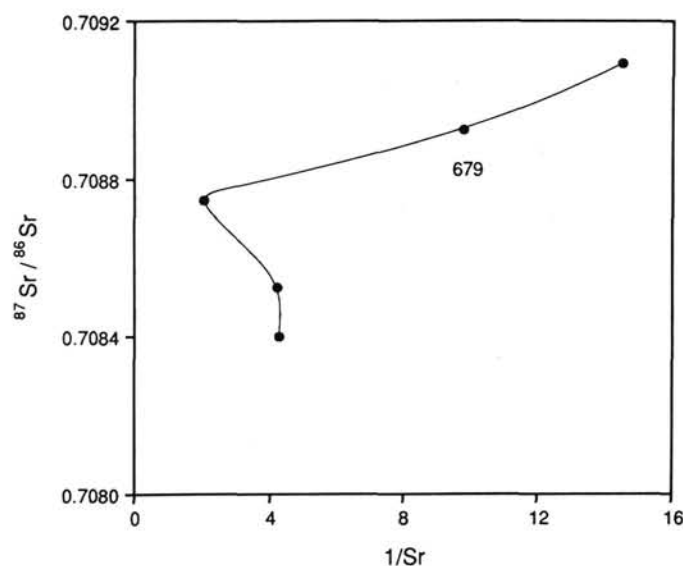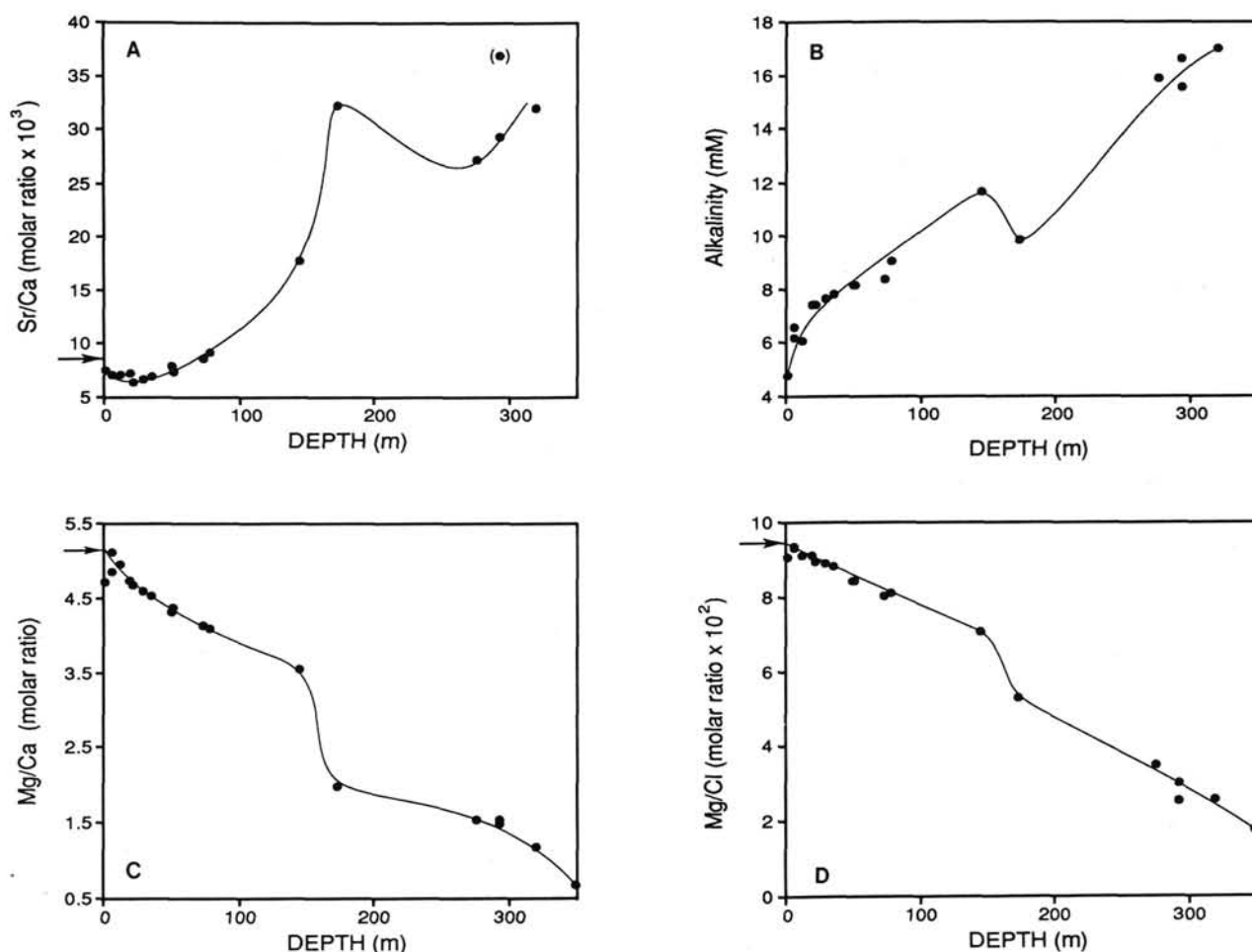
Figure 24. Depth profiles in interstitial waters of molar ratios. A. Sr^{2+}/Ca^{2+}. B. Alkalinity. C. Mg^{2+}/Ca^{2+}. D. Mg^{2+}/Cl^-. (For Site 679.)

sedimentation rates of >100 m/m.y., by high organic carbon content, averaging 2% to 4%, and by the ubiquitous presence of gas hydrates (Suess, von Huene, et al., 1988; Kvenvolden and Kastner, this volume). The average geothermal gradient is 43°C/km in the region of 9°S, and 50°C/km in the region of 11°S (Yamano and Uyeda, this volume; Kvenvolden and Kastner, this volume).

The most distinctive characteristic of the interstitial-water chemistry at the slope sites is the presence of strong negative chloride gradients with depth. The minimum measured value of 454 mM Cl⁻, at the bottom of Site 683 (9°S) at 452 mbsf corresponds to ~20% dilution of seawater chloride. For the purpose of discussion, the northern Sites 683 and 685 (9°S) are considered separately from the more southerly Sites 682 and 688 (11°S) (Fig. 1 and Table 1) because each group shows distinctive chemical and strontium isotopic signatures. The depth profiles of chloride for the interstitial waters of all the slope sites are illustrated in Figure 25. Clearly that the Cl⁻

Table 15. Strontium isotopic composition of bulk solids from Sites 683 and 685, Leg 112.

Core, section, interval (cm)	Depth (mbsf)	Ratio
112-683A-15X-1, 140–150	127	0.708802
685A-9X-7, 145–150	80	0.7086
685A-36X-6, 140–150	328	0.7090
685A-50X-1, 92–102	450	0.709199

gradients do not represent simple diffusion profiles; they show nonsteady-state features, exhibiting distinct minima in Cl⁻ concentrations.

Convergent margin systems are typified by fluid migration, which is closely associated with the tectonics of these environments. In particular, in accretionary complexes, porosity loss and pore fluid expulsion during deformation by tectonic compaction and plate subduction have been documented extensively (i.e., Davis et al., 1983; Etheridge et al., 1985; Bray and Karig, 1985, 1986; Fowler et al., 1985). Migration of such fluids, unless modified by mixing with a more dilute fluid, could not explain the origin of these negative chloride gradients, nor provide the source for the similar low-chloride, methane-rich fluids that are venting at the seafloor and supporting prolific benthic communities at several convergent margins (e.g., Suess et al., 1985; Kulm et al., 1986; Ritger et al., 1987; Boulegue et al., 1987).

Possible origins of the low-chloride fluids are (1) gas-hydrate dissociation at depth and subsequent expulsion during tectonic deformation; (2) mineral dehydration, primarily of clay minerals, opal-A, and other oxyhydroxides; and (3) clay membrane ion filtration.

The commonly observed progressive dilution with depth in interstitial waters associated with gas hydrates has been attributed largely to sampling artifacts or to drilling-induced pressure release and consequent hydrate dissociation (Harrison et al., 1982; Hesse et al., 1985). In view of the above-mentioned recent findings of methane-rich, low-chloride flu-

ids, venting at the seafloor in several convergent margin environments, gas-hydrate dissociation below the bottom-simulating reflector (BSR), and upward fluid expulsion during deformation certainly should be considered as important sources of the observed low-chloride fluids.

Although gas hydrates are common in the Peruvian middle- to lower-slope sediments, and dilution effects by gas hydrate dissociation were observed on board ship, the chlorinity profiles and the physical observations of the cores, e.g., fluid-escape structures and others, also support migration of overpressured low-chloride fluids in the accretionary complex and slope sediments. Assuming that gas-hydrate dissociation is the sole reaction responsible for the low-chloride fluids of Tables 8 through 11 and Figures 8 through 11 and Figure 25, the percentage of dilution by gas hydrate at the bottom of the sites is 3%, 9%, 10%, and 10% at Sites 685, 683, 682, and 688, respectively (Kvenvolden and Kastner, this volume).

During Leg 110, however, low-chloride interstitial waters were encountered in the Northern Barbados accretionary complex, but no gas hydrates seem to occur there. Dewatering reactions of clay minerals was invoked as the origin for these low-chloride fluids (Gieskes et al., in press).

Clay minerals transformation and dehydration reactions have been considered among the prime reactions aiding hydrocarbon migration and thus have been thoroughly studied (e.g., Powers, 1967; Burst, 1969; Perry and Hower, 1970; Colten-Bradley, 1987). These important reactions are temperature and pressure dependent, and the H_2O is released noncontinuously. With a geothermal gradient of approximately 50°C/km, as at the Peruvian margin (Yamano and Uyeda; Kvenvolden and Kastner, this volume), a smectite may release its first H_2O molecule at ~800 to 1000 mbsf. The deepest sediments recovered at Site 688 were at 770 mbsf. Thus, Cl^- dilution by clay-minerals dehydration reaction would require advective flow, even at Site 688. Similar considerations may be applied to opal-A dehydration.

The importance of the clay membrane ion filtration reaction in thick clay-rich sediments was suggested by Hanshaw and Coplen (1973) and Coplen and Hanshaw (1973). Experimental work (e.g., by Coplen and Hanshaw, 1973; Kharaka and Berry, 1973; Haydon and Graf, 1986; Phillips and Bentley, 1987) indicates that the efficiency of the process increases with increasing pressure. The second reaction, clay mineral (and other mineral) dehydration, however, would be a more efficient source of low-chloride fluids than clay membrane ion filtration.

Are there distinct geochemical and isotopic signatures that may help to recognize contributions to the interstitial waters from more than one of these possible additional low-chloride fluid sources? Gas-hydrate dissociation should provide a simple dilution signal for almost all the major ion components. Clay membrane ion filtration, however, would affect the ions sequentially (e.g., Coplen and Hanshaw, 1973; Hanshaw and Coplen, 1973; Hayden and Graf, 1986; Phillips and Bentley, 1987). As a first approximation during clay dehydration, at least some ions in the ion-exchange sites would be expected to migrate with the water, but no experimental observations are available on the subject. For oxygen and hydrogen isotopes, it has been shown that these isotopes of gas hydrate water are heavier than those of seawater (e.g., Hesse and Harrison, 1981; Hesse et al., 1985; Kvenvolden and Kastner, this volume). The $\delta^{18}O$ and δD values of a gas-hydrate sample recovered at Site 688 at 141 mbsf are 1.76% and 17.6% (SMOW), respectively. Because this sample was contaminated by ~17% admixed seawater; its Cl^- concentration is 90.6 mM. The extrapolated end-member $\delta^{18}O$ and δD isotopic ratios are 2.4 and 21.8 ‰, respectively (Kvenvolden and

Kastner, this volume). The experiments by Coplen and Hanshaw (1973) and Phillips and Bentley (1987) on isotopic fractionation during clay-membrane ion filtration show that the oxygen in the water on the dilute side is isotopically lighter. Thus, the oxygen isotope ratios may differentiate between these two processes. Although no experimental work on oxygen isotope fractionation during clay dehydration exists, from crystal chemical and statistical mechanical considerations, the water should be isotopically heavier than seawater; hence, it should be shifted in the same direction as by gas-hydrate dissociation.

Sites 683 and 685 (~9°S)

It is important to emphasize that accreted sediments were encountered only at Site 685, where a hiatus of at least 4.3 m.y. exists between the Quaternary slope sediments (0–200 mbsf) and the underlying early to late Miocene accreted complex. Continental crust underlies Site 683 (Suess, von Huene, et al., 1988; von Huene, this volume). The three striking features of the interstitial-water chemistry of these sites are (1) the very steep and nonsteady-state Cl^- depth profile at Site 683 (Fig. 25A), (2) the distinctly non steady-state profile of $^{87}Sr/^{86}Sr$ ratios at Site 685 (Fig. 26A), and (3) the
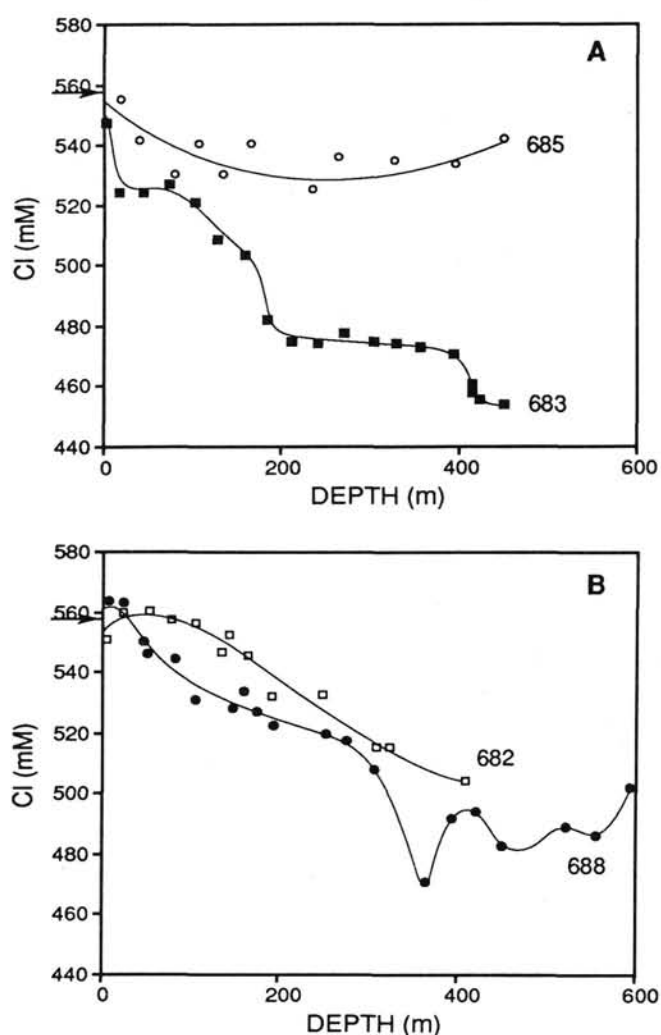

Figure 25. Depth profiles of chloride concentrations in interstitial waters. A. Sites 683 and 685 at ~9°S. B. Sites 682 and 688 at ~11°S.
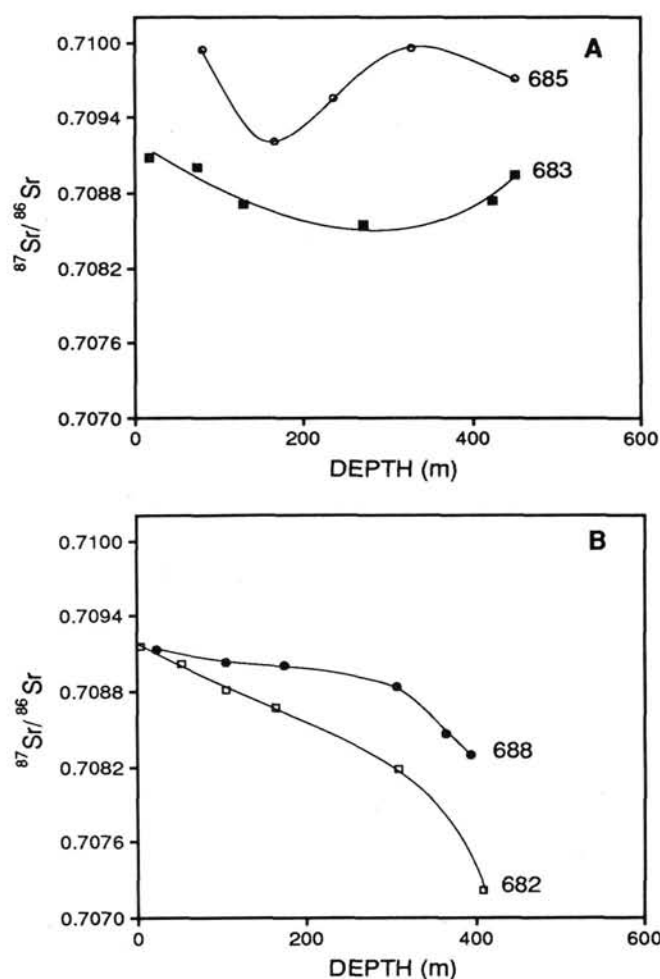
Figure 26. Depth profiles of $^{87}Sr/^{86}Sr$ ratios of interstitial waters. A. Sites 683 and 685. B. Sites 682 and 688.

Figure 27. Depth profiles of chloride concentrations in interstitial waters. A. Site 688; also shown is age of sediment section, positions of unconformities (horizontal lines and arrows), location of bottom simulating reflector (BSR), and estimated geothermal gradient. B. Site 674 in the Barbados accretionary complex (from Moore, Mascle, et al., 1987); also shown are locations of faults (horizontal lines).

$^{87}Sr/^{86}Sr$ ratios extend to values higher than for present-day seawater, especially at Site 685 (Fig. 26A and Table 12).

These three aspects are most likely to be related to the migration of fluids in the tectonically active environments of these two sites. The three Cl$^-$ dilution spikes at Site 683, which occur within the gas hydrates zone, suggest lateral flow of low-chloride fluids. The possible origins of such fluids were discussed earlier. It is clear that at such shallow burial depths and low temperatures, except for some dilution by gas hydrate dissociation, these low-chloride fluids must have originated at greater depths than sampled. Both the shallowest and deepest Cl$^-$ dilution spikes, at 15 to 45 and >400 mbsf, respectively, are reflected as well in the Na$^+$ profile, but, as expected, not in the Na$^+$/Cl$^-$ depth profile (Fig. 9). The latter, deepest Cl$^-$ spike corresponds with a major hiatus between the middle Eocene shelf sediments and the middle Miocene slope section, and is thus consistent with fluid migration along a stratigraphically controlled conduit. The center spike at ~200 mbsf cannot be seen in the Na$^+$ profile because at this depth Na$^+$ concentrations are strongly influenced by ion exchange with NH$_4^+$, as indicated by the maxima in the NH$_4^+$ and Na$^+$/Cl$^-$ depth profiles (Fig. 9). Dewatering veins were first observed at about this depth (Suess, von Huene, et al., 1988, "Site 683" chapter). Diffusive response to the stratigraphically controlled lateral low-chloride fluid flow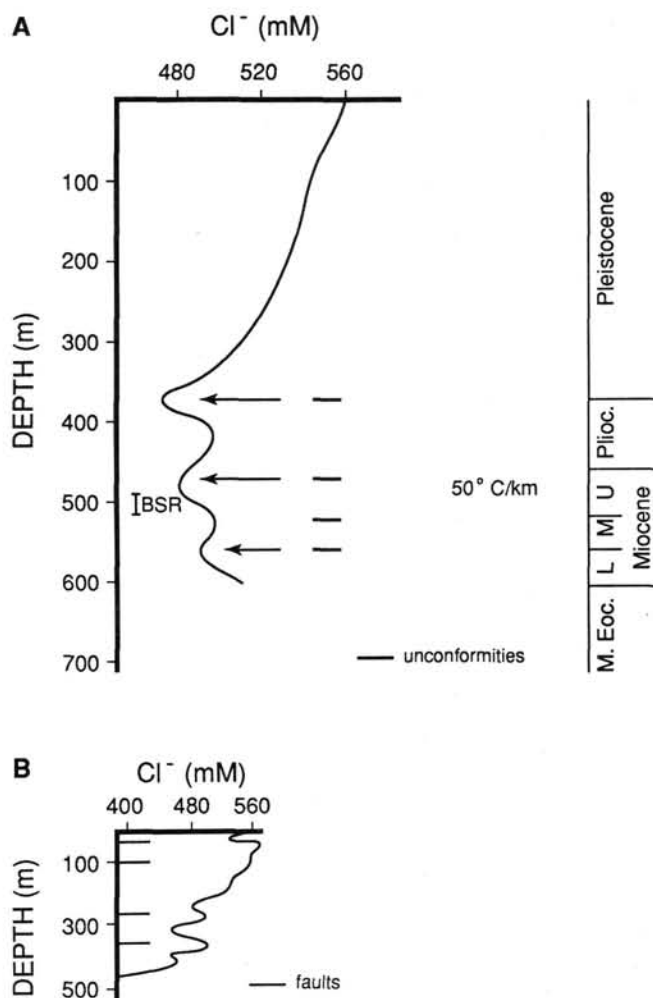 is the most likely cause for the progressive dilution in Cl$^-$ with depth, seen at Sites 683 and 688 (Figs. 25A and 25B, respectively).

The oxygen and hydrogen isotopes of the interstitial waters at Site 683 are negative relative to SMOW (Table 13), and considerably lower than the values expected for interstitial waters modified by gas-hydrate dissociation and/or clay-mineral dehydration. Both reactions would provide heavier than seawater oxygen and hydrogen isotopic values to the interstitial waters. Clearly, an additional source of a fluid with lighter than seawater oxygen and hydrogen isotopes exists. As yet its origin is undefined.

Depth profiles of $^{87}Sr/^{86}Sr$ ratios for these sites are illustrated in Figure 26A. Radiogenic $^{87}Sr/^{86}Sr$ ratios of interstitial water, such as recorded here, are extremely unusual (Elderfield and Gieskes, 1982). They would seem to indicate fluid penetration of and reaction with either the underlying continental crust or with radiogenic clastic sediments. Preliminary strontium isotopic analyses of a number of bulk sediment samples do not reveal ratios as high as those recorded in the interstitial waters (Table 15). The two deepest samples at Site 685 (Table 15) are carbonate-free. At Site 685, observations of higher heat-flow values at shallow
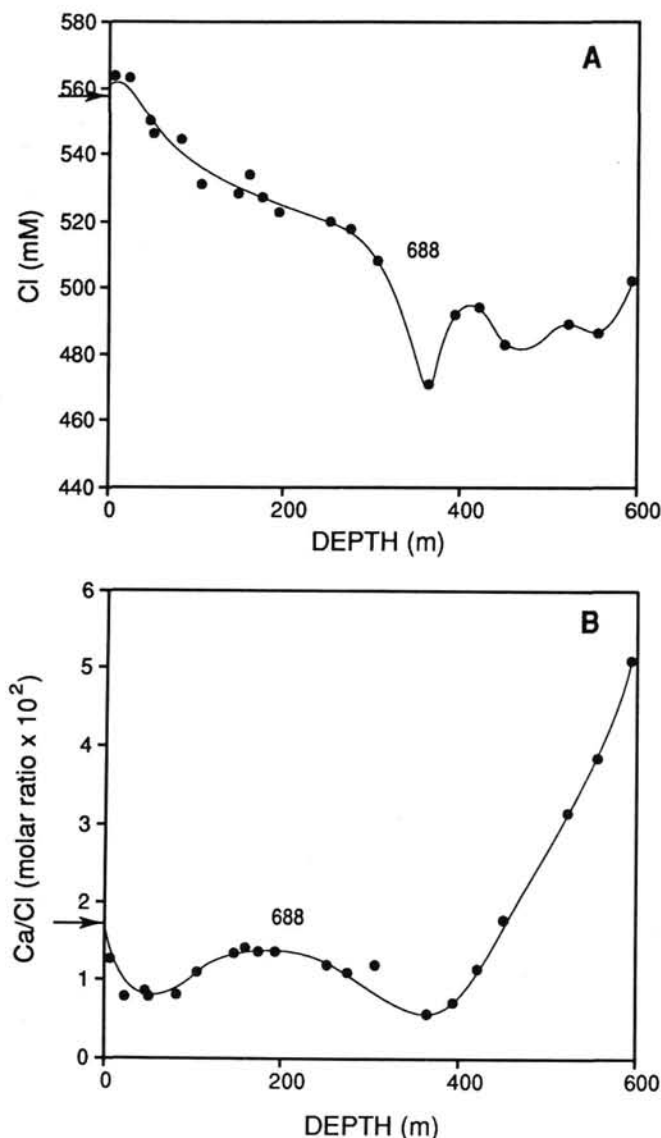
Figure 28. Depth profiles in interstitial waters of Site 688. A. Chloride concentrations. B. Molar Ca^{2+}/Cl^- ratios.
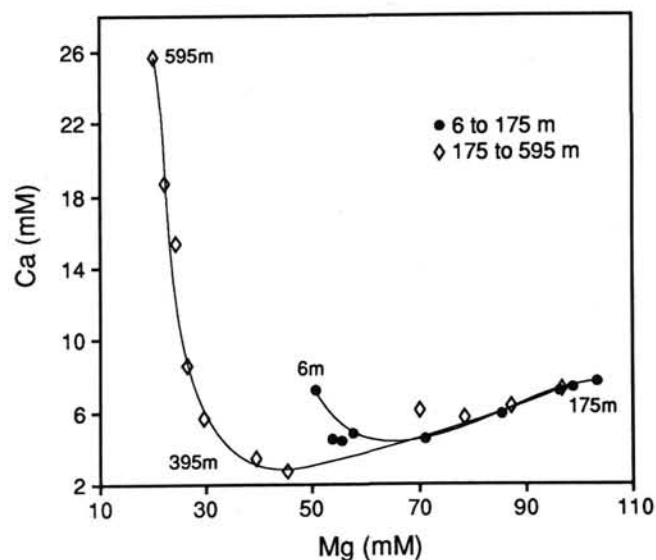

Figure 29. Plots of concentrations of calcium vs. magnesium in interstitial waters of Site 688. Separate lines distinguish samples frommore than 6 to 175 m from those more than 175 to 395 m.

depths, from 0 to 75 mbsf, than at greater depths, at 75 to 150 mbsf (Yamano and Uyeda, this volume), are also consistent with advective flow.

Sites 682 and 688 (~11°S)

Shelf to upper bathyal depth Eocene sediments occur at the bottom of both sites; thus, the continental crust extends to the lower slope (Suess, von Huene, et al., 1988). It is also interesting to note that although the age of the subducting plate beneath these sites south of the Mendaña Fracture Zone is ~10 m.y. older than north of it (where Sites 683 and 685 are located), heat flow is in fact higher (50°C/km vs. 43°C/km, respectively, Yamano and Uyeda; Kvenvolden and Kastner, this volume).

The most distinctive features of the interstitial-water chemistry of these sites are as follows:

1. The nonsteady-state Cl^- depth profile at Site 688, and particularly the conspicuous Cl^- dilution spike at ~350 m, which is the depth of the unconformity between Pliocene and Pleistocene sediments (Figs. 25B and 27), are consistent with stratigraphically controlled fluid migration. The similarities between the Cl^- depth profiles of this site (Fig. 27A) and that of Site 674, at the Barbados Ridge (Fig. 27B), are striking. The Cl^- dilution spike at ~350 mbsf, as well as the deeper ones, indicates active fluid flow, years.

2. A corresponding striking break in the Ca^{2+}/Cl^- vs. depth profile, in the Ca^{2+} vs. Mg^{2+} profile (Figs. 28 and 29) and the steep slope of the latter profile below ~350 mbsf of C^{2+}/Mg^{2+} of almost −3, illustrated in Figure 29. Similar gradients typify seawater modified by interaction with oceanic crust (e.g., McDuff and Gieskes, 1976; McDuff, 1981; Edmond et al., 1979). Extrapolation to 0 Mg^{2+} is reached at ~1000 mbsf. This observation is consistent with recent findings by Jeffrey et al. (1988) of the association of mantle helium with gases from several convergent plate margins.

3. The negative $\delta^{18}O$ and δD values of −1.2 and −8.5 ‰ (SMOW), respectively, of the low Cl^- interstitial waters at Site 688 (Table 15), at a depth of 100 m above the BSR depth in this region (Kvenvolden and Kastner, this volume), strongly suggest that an additional source of an isotopically light fluid, other than the residual water from the formation of gas hydrates, is present. Its source is uncertain. Influence by meteoric water cannot be excluded, but is perplexing so near the trench. The assumption that the origin of the low Cl^- concentration of the interstitial waters is largely from dissociation of gas hydrates and from dehydration of clay minerals constrains the proportion of the isotopically light fluid that is present.

4. The $^{87}Sr/^{86}Sr$ depth profiles (Fig. 26B), contrast very strongly with those from the 9°S slope sites (Fig. 26A) in that they exhibit low $^{87}Sr/^{86}Sr$ ratios, down to 0.7072 at Site 682. Such low values are uncommon for sediments of these ages and require a pool of nonradiogenic strontium. Extrapolation to MORB $^{87}Sr/^{86}Sr$ ratio is reached at the extrapolated 0 Mg^{2+} depth, of ~1000 mbsf.

Carbonate Diagenesis

The interstitial waters at two slope sites, 685 (9°S) and 688 (11°S), the closest ones to the trench, with sedimentation rates of >100 m/m.y., exhibit record alkalinities (max. 266 mM), ammonia (max. 63 mM), and phosphate (max. 826 mM) concentrations (Tables 8 through 11 and Figs. 8
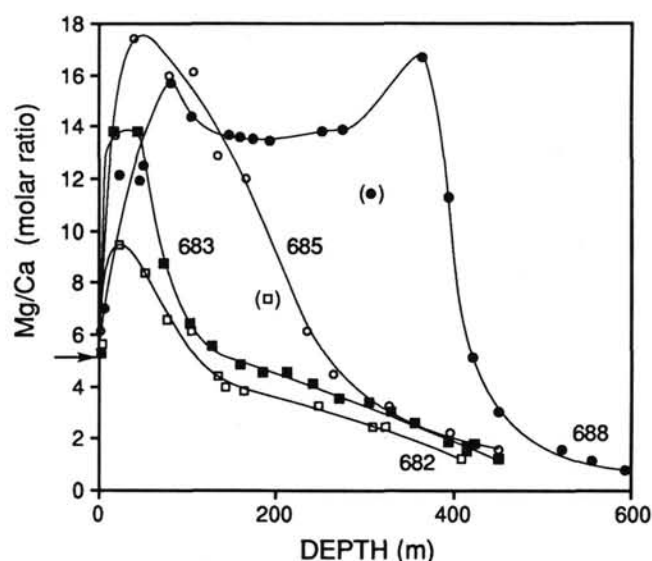
Figure 30. Depth profiles in interstitial waters of Mg^{2+}/Ca^{2+} molar ratios for slope Sites, 682, 683, 685, and 688.

through 11). Despite the extremely high alkalinities in the interstitial waters of all slope sites, the abundance of authigenic carbonates is significantly lower than at the shelf sites. Clearly, the availability of Ca^{2+} and/or of Mg^{2+} and not of bicarbonate limit authigenic carbonate formation at these sites. Diffusional communication with seawater ceases rapidly at shallow (<20–30 m) burial depths in such rapid sedimentation regimes.

Although evidence for fluid advection exists at all slope sites, the transport of solutes required for diagenesis depends on the source-fluid chemistry and on the lithology and structural geology. Fluid flow through horizons having high intergranular permeability seems important in coarser-grained sediments (Kulm et al., 1986a; Thornburg and Suess, this volume), and in finer-grained sediments fluid migration and expulsion along fracture permeability associated with faults apparently dominates (Moore, Mascle, et al., 1987). The Cl^- depth profiles suggest that, at least at the slope Sites 683 and 688, the fluid transport is stratigraphically controlled (Fig. 26) and that the migrating fluids are more dilute than seawater. It thus appears that most of the sediment section is not necessarily significantly influenced by large-scale fluid flow.

As at the shelf sites, at all the slope sites calcite crystallization kinetically precedes dolomite formation. The rate of dolomite formation markedly increases with increasing interstitial water Mg^{2+}/Ca^{2+} ratios, bicarbonate concentrations and decreasing SO_4^{2-} concentrations. Mg^{2+}/Ca^{2+} maxima of 9.2 to 16.7 were observed (Fig. 30 and Tables 8 through 11). At the shelf sites, 7.3 was the maximum Mg^{2+}/Ca^{2+} ratio. The Mg^{2+}/Ca^{2+} depth profiles trend toward lower values, and co-formation of calcite and dolomite ensues at depth. Small amounts of authigenic manganese and iron-rich carbonates also exist at these sites.

Summary of Slope Sites

The chemistry and isotopic compositions of the interstitial waters provide insight into the regional multiple sources of elements of the sediment-water system. On the slope the sites are influenced by low-chloride fluids. Strontium isotope data reveal two separate hydrogeochemical regimes: the more northerly one is influenced by fluids having a radiogenic strontium signature, whereas the more southerly one is influenced by fluids having a nonradiogenic signature. Con-

sidering the complexities of this environment, evaluation of the interrelations between the shelf and slope hydrogeochemical regimes is precluded at this time. Future work on minor- and trace-element concentrations and on additional isotopic ratios of the fluids and solids may elucidate this problem.

REFERENCES

Baker, P. A., and Burns, S. J., 1985. Occurrence and formation of dolomite in organic-rich continental margin sediments. *AAPG Bull.*, 69:1917–1930.

Baker, P. A., and Kastner, M., 1981. Constraints on the formation of sedimentary dolomite. *Science*, 213:214–216.

Barnes, R. O., 1988. ODP in situ fluid sampling and measurement: a new wireline tool. *In* Mascle, A., Moore, J. L., et al., *Proc. ODP, Init. Repts.*, 110: College Station, TX, (Ocean Drilling Program), 55–63.

Bischoff, J. L., Clancy, J. J., and Booth, J. S., 1975. Magnesium removal in reducing marine sediments by cation exchange. *Geochim. Cosmochim. Acta*, 39:559–568.

Brantley, S. L., Moller, N. E., Crerar, D. A., and Weare, J. H., 1984. Geochemistry of a modern evaporite: Bocana de Virrila, Peru. *J. Sediment. Petrol.*, 54:447–462.

Boulegue, J., Iiyama, J. T., Charleu, J. L., and Jedwab, J., 1987. Nankai Trough, Japan Trench and Kuril Trench: Geochemistry of fluid samples by submersible "Nautile." *Earth Planet. Sci. Lett.*, 83:362–375.

Braitsch, O., 1971. Salt Deposits, Their Origin and Composition: Berlin Heidelberg (Springer-Verlag), 297.

Bray, C. J., and Karig, D. E., 1985. Porosity of sediments in accretionary prisms and some implications for dewatering processes. *J. Geophys. Res.*, 90:768–778.

————, 1986. Physical properties of sediments from the Nankai Trough, DSDP Leg 87A, Sites 582 and 583. *In* Kagami, H., Karig, D. E., et al., *Init. Repts. DSDP*, 87: Washington (U.S. Govt. Printing Office), 827–842.

Broecker, W., and Peng, T.-S., 1982. Tracers in the Sea: Palisades, NY (Columbia Univ. Press), 690.

Burst, J. F., 1969. Diagenesis of Gulf Coast clayey sediments and its possible relation to petroleum migration. *AAPG Bull.*, 53:73–93.

Carpenter, A. B., 1978. Origin and Chemical Evolution of Brines in Sedimentary Basins. *Oklahoma Geol. Surv. Circ.*, 79:60-77.

Claypool, G. E., and Kaplan, L. R., 1974. The origin and distribution of methane in marine sediments. *In* Kaplan, I. R. (Ed.), *Natural Gases in Marine Sediments:* New York (Plenum Press), 99–139.

Cloos, M., 1984. Landward dipping reflectors in accretionary wedges: active dewatering conduits? *Geology*, 12:519–522.

Colten-Bradley, V. A., 1987. Role of pressure in smectite dehydration—Effects on geopressure and smectite-to-illite transformation. *AAPG Bull.*, 71:1414–1427.

Coplen, T. B., and Hanshaw, B. B., 1973. Ultrafiltration by compacted clay membrane—1. Oxygen and hydrogen isotopic fractionation. *Geochim. Cosmochim. Acta*, 37:2295–2310.

Craig, H., and Gordon, L. I., 1965. Deuterium and oxygen 18 variations in the ocean and the marine atmosphere. *In Stable Isotopes in Oceanographic Studies and Paleotemperatures:* Spoleto (Consiglio Nazionale delle Ricerche, Pisa), 9–130.

Davis, D., Suppe, J., and Dahlen, F. A., 1983. The mechanics of fold-and-thrust belts. *J. Geophys. Res.*, 88:1153–1172.

Edmond, J. M., Measures, C. I., McDuff, R. E., Chan, L. H., Collier, R., Grant, B., Gordon, L. I., and Corliss, J., 1979. Ridge crest hydrothermal activity and the balances of the major and minor elements in the ocean: the Galapagos data. *Earth Planet. Sci. Lett.*, 46:1–18.

Elderfield, H., 1986. Strontium isotope stratigraphy. *Palaeogeogr. Palaeoclimatol. Palaeoecol.*, 57:71–90.

Elderfield, H., and Gieskes, J. M., 1982. Sr isotopes in interstitial waters of Deep Sea Drilling Project cores. *Nature*, 300:493–497.

Etheridge, M. A., Wall, V. J., and Vernon, R. H., 1983. The role of the fluid phase during regional metamorphism and deformation. *J. Metamorph. Geol.*, 1:205–226.

Eugster, H. P., and Jones, B. F., 1979. Behavior of major solutes during closed-basin brine evolution. *Am. J. Sci.*, 279:609–631.

Faure, G., 1986. *Principles of Isotope Geology:* New York (Wiley), 589.

Fowler, S. R., White, R. S., and Louden, K. E., 1985. Sediment dewatering in the Makran accretionary prism. *Earth Planet. Sci. Lett.*, 75:427–438.

Garrison, R. E., Kastner, M., and Zenger, D. H. (Eds.), 1984. *Dolomites of the Monterey Formation and Other Organic-Rich Units*. Soc. Econ. Paleontol. Mineral., Pac. Sec. 41:215.

Gieskes, J. M., 1973. Interstitial water studies, Leg 15, alkalinity, pH, Mg, Ca, Si, PO_4 and NH_4. *In* Heezen, B. C., MacGregor, I. D., et al., *Init. Repts. DSDP*, 20: Washington (U.S. Govt. Printing Office), 813–829.

_____, 1975. Chemistry of interstitial waters of marine sediments. *Annu. Rev. Earth Planet. Sci.*, 3:433–453.

Gieskes, J. M., Blanc, G., Vrolijk, P., Elderfield, H., and Barnes, R., in press. Interstitial water chemistry-major constituents, Leg 110. *In* Mascle, A., Moore, J. C., et al., *Proc. ODP, Sci. Results*, 110: College Station, TX (Ocean Drilling Program).

Gieskes, J. M., Elderfield, H., and Palmer, M. R., 1986. Strontium and its isotopic composition in interstitial waters of marine carbonate sediments. *Earth Planet. Sci. Lett.*, 77:229–235.

Gieskes J. M., and Peretsman, G., 1986. *Water-chemistry Procedures Aboard JOIDES Resolution.—Some Comments:* College Station, TX (Ocean Drilling Program), Tech. Note No. 5:46.

Hanshaw, B. B., and Coplen, T. B., 1973. Ultrafiltration by compacted clay membrane. II. Sodium ion exclusion at various ionic strengths. *Geochim. Cosmochim. Acta*, 37:2311–2327.

Harrison, W. E., Hesse, R., and Gieskes, J. M., 1982. Relationship between sedimentary facies and interstitial water chemistry of slope, trench, and Cocos plate site from the Middle American Trench transect, DSDP Leg 67. *In* Aubouin, J., von Huene, R., et al., *Init. Repts. DSDP*, 67: Washington (U.S. Govt. Printing Office), 603–614.

Haydon, P. R., and Graf, D. L., 1986. Studies of smectite membrane behavior: temperature dependence, 20°–180°C. *Geochim. Cosmochim. Acta*, 50:115–121.

Hesse, R., and Harrison, W. E., 1981. Gas-hydrates (clathrates) causing pore-water freshening and oxygen isotope fractionation in deep-water sedimentary sections of the terrigenous continental margins. *Earth Planet. Sci. Lett.*, 55:453–462.

Hesse, R., Lebel, J., and Gieskes, J. M., 1985. Interstitial water chemistry of gas-hydrate-bearing sections of the middle America Trench slope, DSDP Leg 84. *In* von Huene, R., Aubouin, J., et al., *Init. Repts. DSDP*, 84: Washington (U.S. Govt. Printing Office), 727–737.

Holser, W. T., 1979a. Mineralogy of evaporites. *In* Burns, R. G. (Ed.), *Marine Minerals; Reviews in Minerals, Vol. 6:* New York (Mineral. Soc. Am.), 211–294.

_____, 1979b. Trace elements and isotopes in evaporites. *In* Burns, R. G. (Ed.), *Marine Minerals; Reviews in Minerals, Vol. 6:* New York (Mineral. Soc. Amer.), 295–346.

Hussong, D. M., Edwards, P. B., Johnson, S. H., Campbell, J. F., and Sutton, G. H., 1976. Crustal Structure of the Peru-Chile Trench: 8°S to 12°S Latitude. *Am. Geophys. Union Mono.*, 19:71–86.

Hussong, D. M., and Wipperman, L. K., 1981. Vertical movement and tectonic erosion of the continental wall of the Peru-Chile Trench near 11°30'S latitude. *In* Kulm, L. D., Dymond, J., Dasch, E. J., Hussong, D. M., and Roderick, R. (Eds.), *Nazca Plate: Crustal Formation and Andean Convergence*. Geol. Soc. Am. Mem., 154:509–524.

Illing, L. V., Wells, A. J., and Taylor, J.C.M., 1965. Penecontemporary Dolomite in the Persian Gulf. *Soc. Econ. Paleontol. Mineral. Spec. Publ.*, 13.

Jeffrey, A., Kaplan, I., Poreda, R., and Craig, H., 1988. The origin of natural gases from convergent margins. *V. M. Goldschmidt Confer. Geochem. Soc.*, 49.

Kastner, M., 1981. Authigenic silicates in deep-sea sediments: formation and diagenesis. *In* Emiliani, C. (Ed.), *The Sea, Vol. 7:* New York (Wiley), 915–980.

Kastner, M., Suess, E., Garrison, R. E., and Kvenvolden, K., 1987. Hydrology, geochemistry and diagenesis along the convergent margin off Peru. *EOS*, 68:1499.

Kastner, M., Martin, J., Suess, E., Garrison, R. E., and Kvenvolden, K., 1988. Evidence for density and tectonically driven fluid migration in convergent margin sediments off Peru. *EOS*, 69:1263.

Kharaka, Y. K., and Berry, F.A.F., 1973. Simultaneous flow of water and solutes through geological membranes—1. Experimental investigation. *Geochim. Cosmochim. Acta*, 37:2577–2603.

Kulm, L. D., Prince, R. A., French, W., Johnson, S., and Masias, A., 1981. Crustal structure and tectonics of the central Peru continental margin and trench. *In* Kulm, L. D., Dymond, J., et al., (Eds.), *Nazca Plate: Crustal Formation and Andean Convergence*. Geol. Soc. Am. Mem., 154:445–468.

Kulm, L. D., Suess, E., Thornburg, T. M., Embly, R. W., Hussong, D. M., and Resig, J. M., 1986. Fluid venting processes and their relation to tectonic styles in subduction zones of the eastern Pacific. *Proc. Int. Kaiko Conf. Subduction Zones*, 28–29.

Kulm, L. D., Suess, E., Moore, J. C., Carson, B., Lewis, B. T., Ritger, S. D., Kadko, D. C., Thornburg, T. M., Embley, R. W., Rugh, W. D., Massoth, G. J., Langseth, M. G., Cochrane, G. R., and Seamman, R. L., 1986. Oregon subduction zone: venting, sauna and carbonates. *Science*, 231:561–566.

Langseth, M. G., Westbrook, G. K., and Hobart, M. A., 1988. Geophysical survey of a mud volcano seaward of the Barbados Ridge accretionary complex. *J. Geophs. Res.*, 93:1049–1061.

Lippman, F., 1973. *Sedimentary Carbonate Minerals:* New York-Berlin-Heidelberg (Springer-Verlag), 288.

Lloyd, R. M., 1966. Oxygen isotope enrichment in seawater by evaporation. *Geochim. Cosmochim. Acta*, 30:801–814.

Mackin, J. E., and Aller, R. C., 1984. Ammonium adsorption in marine sediments. *Limnol. Oceanogr.*, 29:250–257.

Manheim, F. T., and Sayles, F. L., 1974. Composition and origin of interstitial waters of marine sediments, based on deep sea drill cores. *In* Goldberg, E. D. (Ed.), *The Sea, Vol. 5:* New York (Wiley Interscience), 527–568.

McCaffrey, M. A., Lazar, B., and Holland, H. D., 1987. The evaporation path of seawater and the coprecipitation of Br and K^+ with halite. *J. Sediment. Petrol.*, 57:928–937.

McDuff, R. E., 1981. Major cation gradients in DSDP interstitial waters: the role of diffusive exchange between seawater and the upper crust. *Geochim. Cosmochim. Acta*, 45:1701–1715.

McDuff, R. E., and Gieskes, J. M., 1976. Calcium and magnesium profiles in DSDP interstitial waters: diffusion or reaction? *Earth Planet. Sci. Lett.*, 33:1–10.

Miller, J., Hussong, D., and von Huene, R., 1986. Peru continental margin, record section 3. *In* von Huene, R. (Ed.), *Seismic Images of Modern Convergent Margin Tectonic Structure*. AAPG Studies in Geol. Ser., 26:32–33.

Millero, F. J., 1974. Seawater as a multicomponent electrolyte solution. *In* Goldberg, E. D. (Ed.), *The Sea, Vol. 5:* New York (Wiley), 3–80.

Millero, F. J., and Schreiber, D. R., 1982. Use of the ion pairing model to estimate activity coefficients of the ionic components of natural waters. *Am. J. Sci.*, 282:1508–1540.

Moore, J. C., Mascle, A., and Leg 110 Shipboard Scientists, 1987. Expulsion of fluids from depths along a subduction zone décollement horizon. *Nature*, 326:785–788.

Morris, R. C., and Dickey, P. A., 1959. Modern evaporite deposition in Peru. *AAPG Bull.*, 41:2467–2474.

Noble, D. C., McKee, E. H., and Megard, F., 1979. Early Tertiary "Incaic" tectonism, uplift, and volcanic activity, Andes of central Peru. *Geol. Soc. Am. Bull.*, 90:903–907.

Perry, E., and Hower, J., 1970. Burial diagenesis in Gulf Coast pelitic sediments. *Clays and Clay Minerals*, 18:165–177.

Phillips, F. M., and Bentley, H. W., 1987. Isotopic fractionation during ion filtration: 1. Theory. *Geochim. Cosmochim. Acta,* 51:683–695.

Powers, N. C., 1967. Fluid release mechanisms in compacting marine mudrocks and their importance in oil exploration. *AAPG Bull.,* 51:1240–1254.

Reck, B. H., 1987. Implications of measured thermal gradients for water movement through the northeast Japan accretionary prison. *J. Geophys. Res.,* 92:3683–3690.

Ritger, S., Carson, B., and Suess, E., 1987. Methane-derived authigenic carbonates formed by subduction-induced pore water expulsion along the Oregon/Washington margin. *Geol. Soc. Am. Bull.,* 48:147–156.

Rosenfeld, J. K., 1979. Ammonium absorption in nearshore anoxic sediments. *Limnol. Oceanogr.,* 24:356–364.

Sayles, F. L., 1970. Preliminary geochemistry. *In* Bader, R. G., Gerard, R. D., et al., *Init. Repts. DSDP,* 4: Washington (U.S. Govt. Printing Office), 645.

Sayles, F. L., and Mangelsdorf, P. C., 1977. The equilibrium of clay minerals with seawater. *Geochim. Cosmochim. Acta,* 41:951–960.

Shearman, D. J., 1963. Recent anhydrate gypsum, dolomite and halite from the coastal states of the Arabian shore of the Persian Gulf. *Proc. Geol. Soc. London.,* 607:63–65.

Suess, E., Carson, B., Ritgar, S., Moore, J. C., Jones, M. L., Kulm, L. D., and Cochrane, G. R., 1985. Biological communities at vent sites along the subduction zone off Oregon. *Biol. Soc. Wash. Bull.,* 6:475–484.

Suess, E., von Huene, R., et al., 1988. *Proc. ODP, Init. Repts.,* 112: College Station, TX. (Ocean Drilling Program).

Suess, E., von Huene, R., and Leg 112 Shipboard Scientists, 1988. Ocean Drilling Program Leg 112; Peru Continental Margin: Part 2,

Sedimentary history and diagenesis in a coastal upwelling environment. *Geology,* 16:939–943.

Thornburg, T. M., and Kulm, L. D., 1981. Sedimentary basins of the Peru continental margin: structure, stratigraphy and Cenozoic tectonics from 6°S to 16°S latitude. *In* Kulm, L. D., Dymond, J., Dasch, E. J., Hussong, D. M., and Roderick, R. (Eds.), *Nazca Plate: Crustal Formation and Andean Convergence.* Geol. Soc. Am. Mem., 154:393–422.

Usiglio, M. J., 1849. Etudes sur la composition de l'eau de la Mediterranée et sur l'exploitation des sel qu'ele continent. *Annu. Chim. Phys.,* 27:172–191.

von Huene, R., Kulm, L. D., and Miller, J., 1985. Structure of the frontal part of the Andean convergent margin. *J. Geophys. Res.,* 90:5429–5442.

von Huene, R., and Miller, J., 1988. Erosion and accretion along the southern Peru Margin. *EOS,* 69:1406.

von Huene, R., Suess, E., and Leg 112 Shipboard Scientists, 1988. Results of Leg 112 drilling, Peru continental margin: Part 1, tectonic history. *Geology,* 16:934–938.

Whiffield, M., 1974. The hydrolysis of ammonium ions in seawater—a theoretical study. *J. Mar. Biol. Assoc. U.K.,* 54:565–580.

Zherebtsova, I. K., and Volkova, N. N., 1966. Experimental study of behaviour of trace elements in the process of natural solar evaporation of Black Sea Water and Sasyk-Sivash brine. *Geochem. Int.,* 3:656–670.

APPENDIX A
Uncontaminated interstitial-water samples, Leg 112.

Core, section, interval (cm)	Depth (mbsf)
112-679C-1H-1, 140–150	1.4
C-1H-4, 140–150	5.9
D-1H-4, 140–150	5.9
C-2H-2, 128–138	11.8
C-3H-1, 140–150	19.9
D-3H-3, 140–150	21.8
C-4H-1, 140–150	29.4
C-4H-5, 140–150	35.4
D-6H-3, 140–150	50.3
C-6H-3, 135–145	51.3
C-8H-5, 140–150	73.4
D-9H-3, 140–150	78.8
D-17X-1, 140–150	143.8
680C-1H-1, 130–150	1.3
B-1H-2, 145–150	3.0
C-1H-3, 145–150	4.5
C-2H-3, 140–150	10.2
C-3H-2, 145–150	18.3
B-3H-3, 145–150	19.5
B-6H-3, 145–150	47.5
B-8H-1, (*in-situ*)	62.5
B-9H-4, 140–150	77.9
B-23H-1, (*in-situ*)	195.5
681C-1H-1, 145–150	1.5
B-1H-2, 145–150	3.0
C-1H-3, 145–150	4.5
C-2H-1, 140–150	7.4
C-2H-4, 145–150	11.9
B-3H-3, 145–150	19.8
C-4H-2, 145–150	27.9
C-4H-5, 145–150	32.4
C-5H-3, 145–150	38.9
C-7H-2, 140–150	56.3
C-8H-1, 140–150	65.8
B-9H-1, 140–150	73.8
C-9H-2, 140–150	75.3

Appendix A (continued).

Core, section, interval (cm)	Depth (mbsf)
B-12X-3, 140–150	98.9
B-15X-1, 135–145	126.0
682A-1H-3, 145–150	4.5
A-3H-3, 140–150	23.7
683A-1H-1, 145–150	1.5
A-30X-2, 74–79	270.4
A-33X-5, 145–150	304.2
A-36X-3, 140–150	329.6
A-39X-2, 140–150	356.6
A-45X-4, 140–150	415.6
683B-3X-2, 140–150	424.4
B-6X-2, 51–63	452.0
684B-1H-3, 145–150	4.5
C-1H-3, 145–150	4.5
C-2H-3, 145–150	12.3
B-3H-3, 145–150	21.5
C-3H-3, 145–150	21.8
C-4H-6, 145–150	35.8
C-5H-1, 145–150	37.8
C-6X-1, 145–150	40.5
C-8X-2, 92–97	60.4
C-13X-1, 140–145	106.9
685A-1H-2, 145–150	3.0
A-3H-3, 145–150	18.1
A-6X-4, 145–150	40.1
A-9X-7, 145–150	79.6
A-12X-5, 145–150	106.6
A-15X-4, 140–150	133.5
A-18X-6, 145–150	165.1
A-27X-1, 120–130	234.8
A-30X-2, 127–137	264.9
A-36X-6, 140–150	328.0
A-44X-3, 40–50	396.0
A-50X-1, 92–102	450.5
686B-1H-3, 145–150	4.5
B-2H-3, 145–150	13.0

Appendix A (continued).

Core, section, interval (cm)	Depth (mbsf)
B-3H-3, 145–150	22.5
B-5H-3, 145–150	41.5
B-6X-2, 145–150	49.5
B-9X-6, 145–150	84.0
B-12X-2, 145–150	106.5
A-14X-1, (*in-situ*)	110.7
B-15X-5, 140–150	139.5
B-18X-4, 140–150	166.4
A-22X-1, (*in-situ*)	186.7
B-24X-2, 140–150	220.4
B-28X-5, 140–150	262.9
B-30X-4, 140–150	280.4
B-32X-2, 140–150	296.4
687B-1H-3, 145–150	4.5
B-3H-4, 140–150	20.6
B-5H-3, 54–64	37.2
B-7H-1, 140–150	54.1
B-15X-1, 140–150	120.7
B-19X-3, 103–113	161.3
A-19X-1, (*in-situ*)	169.0
688A-1H-4, 145–150	6.0
A-3H-4, 145–150	23.8
A-6H-1, (*in-situ*)	46.3
A-6H-3, 145–150	50.8
A-9X-5, 140–150	82.2
A-12X-1, 140–150	104.7
A-16X-4, 140–150	147.2
A-18X-1, (*in-situ*)	160.3
A-19X-3, 140–150	174.2
A-21X-3, 108–118	192.9
A-30X-1, 115–125	275.5
A-33X-3, 140–150	307.2
E-3R-4, 140–150	365.0
E-9R-5, 140–150	422.0

APPENDIX B
Interstitial-water samples corrected for admixed surface seawater introduced by drilling, and calculated percent of admixed seawater, Leg 112.

Core, section, interval (cm)	Depth (m)	SO_4^{2-} (mM)	%Admixed seawater[1]
112-679D-20X-1, 115–125	172.0	1.07	3.70
E-4X-3, 140–150	275.2	1.07	3.70
E-6X-2, 140–150 (mud)	292.7	0.03	0.10
E-6X-2, 140–150 (indurated)	292.7	0.54	1.87
E-9X-CC, (mud)	319.7	0.75	2.60
E-12X-1, 140–150	348.2	1.88	6.51
681A-7H-1, (in-situ)	63.5	1.71	5.92
B-8H-1, (in-situ)	67.0	1.26	4.36
682A-6H-3, 140–150	52.2	4.4	15.22
A-9X-1, 106–116	77.4	2.7	9.34
A-12X-1, 140–150	105.7	2.4	8.30
A-15X-1, 135–139	134.6	3.3	11.42
A-16X-1, (in-situ)	142.8	4.6	15.92
A-18X-1, 145–150	163.3	2.9	10.03
A-21X-1, 130–135	191.6	2.8	9.69
A-27X-1, 106–111	248.4	0.5	1.73
A-34X-2, 140–150	307.5	4.0	13.84
A-36X-1, 140–150	322.1	0.7	5.88
A-46X-1, 140–150	409.6	4.2	14.53
683A-3H-3, 145–150	16.2	2.47	8.55
A-6H-3, 144–150	44.6	1.04	3.60
A-9H-3, 145–150	73.2	1.72	5.95
683A-12X-4, 135–145	103.1	1.97	6.82
A-15X-1, 140–150	127.1	2.08	7.20
A-18X-3, 145–150	158.7	1.10	3.81
A-21X-1, 145–150	184.2	3.97	13.74
A-24X-1, 69–74	211.9	4.42	15.29
A-27X-1, 123–128	240.9	3.10	10.73
A-43X-2, 140–150	393.6	0.95	3.29
B-2X-2, 140–150	414.9	1.13	3.91
684C-7X-2, 145–150	51.5	0.44	1.52
C-10X-1, 35–40	77.4	2.72	9.41
C-11X-1, 145–150	88.0	0.30	1.04
685A-35X-6, 140–150	318.5	1.38	4.78
A-47X-1, 128–138	422.4	2.00	6.92
688A-25X-1, 140–150	228.2	0.66	2.28
A-27X-4, 140–150	251.7	0.23	0.80
E-6R-4, 140–150	393.5	0.46	1.59
E-12R-1, 140–150	450.5	0.32	1.11
E-19R-3, 140–150	521.4	1.24	4.29
E-23R-1, 140–150	556.4	0.54	1.87
E-27R-1, 140–150	594.4	0.32	1.11

[1] Assuming zero sulfate concentration (based on methane data), and calculated on basis of 28.9 mM SO_4 in seawater.